Magneto-enhanced g-C_3N_4/Fe_3O_4 Nanostructures for Photocatalytic Degradation of Amoxicillin and Polystyrene Adsorption in Water

Shambel Tafa Megersa

A Thesis Submitted to the Department of Applied Chemistry

College of Applied Natural Science

Presented in Partial Fulfillment of the Requirement for the Degree of Master's in Physical Chemistry

Office of Graduate Studies

Adama Science and Technology University

October, 2025

Adama, Ethiopia

Magneto-enhanced g-C_3N_4/Fe_3O_4 Nanostructures for Photocatalytic Degradation of Amoxicillin and Polystyrene Adsorption in Water

Shambel Tafa Megersa

Main advisor: Bedasa Abdisa Gonfa (Ph.D)

Co-advisor: Lemma Teshome Tufa (Ph.D)

A Thesis Submitted to the Department of Applied Chemistry

College of Applied Natural Science

Presented in Partial Fulfillment of the Requirement for the Degree of Master's in Physical Chemistry

Office of Graduate Studies

Adama Science and Technology University

October, 2025

Adama, Ethiopia

Declaration

I hereby declare that this Master Thesis entitled **"Magneto-enhanced g-C_3N_4/Fe_3O_4 Nanostructures for Photocatalytic Degradation of Amoxicillin and Polystyrene Adsorption in Water"** is my original work. That is, it has not been submitted for the award of any academic degree, diploma or certificate in any other university. All sources of materials that are used for this thesis have been duly acknowledged through citation

_____	_____	_____
Name of the student	Signature	Date

Recommendation

We, the advisor(s) of this thesis, hereby certify that we have read and revised version of thesis entitled **"Magneto-enhanced g-C_3N_4/Fe_3O_4 Nanostructures for Photocatalytic Degradation of Amoxicillin and Polystyrene Adsorption in Water"** prepared under our guidance by **Shambel Tafa** submitted in partial fulfillment of the requirements for the degree of Mater's of Science in Physical Chemistry. Therefore, we recommend the submission of revised version of the thesis to department following the applicable procedures.

Bedasa Abdisa Gonfa, (PhD)	_____	_____
Major Advisor	Signature	Date
Lemma Teshome Tufa, (PhD)	_____	_____
Co-advisor	Signature	Date

Thesis Approval Sheet

We, the advisors of the thesis entitled "**Magneto-enhanced g-C_3N_4/Fe_3O_4 Nanostructures for Photocatalytic Degradation of Amoxicillin and Polystyrene Adsorption in Water**" and developed by by **Shambel Tafa Megersa,** hereby certify that the recommendation and suggestions made by the board of examiners are appropriately incorporated into the final version of the thesis.

Major Advisor	Signature	Date
Bedasa Abdisa Gonfa, (PhD)	_____	_____
Co-advisor	Signature	Date
Lemma Teshome Tufa, (PhD	_____	_____

We, the undersigned, members of the Board of Examiners of the thesis by **Shambel Tafa Megersa** have read and evaluated the thesis entitled "**Magneto-enhanced g-C_3N_4/Fe_3O_4 Nanostructures for Photocatalytic Degradation of Amoxicillin and Polystyrene Adsorption in Water**" and examined the candidate during open defense. This is, therefore, to certify that the thesis is accepted for partial fulfillment of the requirement of the degree of Master of Science in Physical Chemistry.

_____	_____	_____
Chairperson	Signature	Date
_____	_____	_____
Internal Examiner	Signature	Date
Getachew Adam, PhD		_____
External Examiner	Signature	Date

Final approval and acceptance of the thesis is contingent upon submission of its final copy to the Office of Postgraduate Studies (OPGS) through the Department Graduate Council (DGC) and School Graduate Committee (SGC).

_____	_____	_____
Department Head	Signature	Date
_____	_____	_____
College Dean	Signature	Date
_____	_____	_____
Office of Postgraduate Studies, Dean	Signature	Date

Acknowledgement

First and foremost, I am deeply grateful to Almighty God that has given me the strength and ability to complete this thesis work. Next, I extend my heartfelt thanks to my advisor, Dr. Bedasa Abdisa Gonfa, for being the guiding force behind this work. I am also very grateful to my co-advisor, Dr. Lemma Teshome Tufa, for his invaluable suggestions and amazing support throughout this work. Further, I acknowledges Adama Public Health Research and Referral Laboratory Center (APHRRLC) for providing the amoxicillin (AMX) standard of analytical and laboratory-grade quality. Their kind support is gratefully recognized for contributing to the successful completion of this study. I extend my sincere thanks to my classmates for their friendship and support. Last but not least, I express my appreciation to the members and staff of the Department of Applied Chemistry in the College of Applied Natural Science for their ongoing support and assistance throughout my academic career. Finally, I am kindly grateful to my family for their endless support, prayers, and motivation throughout this endeavor.

Table of contents

List of tables

List of figure

List of acronyms and abbreviations

2D	Two-dimensional
AMX	Amoxicillin
ATs	Antibiotics
CV	Cyclic voltammetry
EIS	Electrochemical Impedance Spectroscopy
FM	Ferrimagnetism
FTO	Fluorine Doped Tin Oxide
g-C_3N_4	Graphitic carbon nitride
MNP	Magnetic nanoparticle
MNS	Magnetic nanostructure
MS	Mott–Schottky
MF	Magnetic field
MPs	Microplastics
PL	Photoluminescence
PZC	Point of zero charge
PS	Polystyrene
SPM	Superparamagnetic

Abstract

The increasing occurrence of microplastics and antibiotics in aquatic environments has become a global concern. Therefore, there is a growing need to development the efficient and cost-effective treatment technologies. This study provides a novel technique that uses synergetic effect of heterojunction and an external magnetic field to enhance both photocatalytic degradation of AMX antibiotic and adsorption of PS microplastics. The Fe_3O_4/g-C_3N_4 magnetic nanostructures (NSs) were synthesized via thermal polymerization followed by the co-precipitation method. The crystal structure, morphology, chemical composition, optical and electrochemical properties of the materials were characterized using X-ray diffraction analysis (XRD), Scanning electron microscopy (SEM), Fourier transform infrared (FTIR), and Ultraviolet-visible (UV-DRS), and electrochemical characterization, which confirmed the successful formation of the g-C_3N_4/Fe_3O_4 heterojunction. The prepared Catalystes were tested for the photodegradation of AMX under visible light irradiation and adsorption of PS. Compared to Pristine Fe_3O_4, and g-C_3N_4 the 0.5 T external magnetic field enhanced g-C_3N_4/Fe_3O_4 MNSs showed greatly improved photocatalytic performances 94.7% at optimum conditions, and the synergetic effect also show boosted adsorption capacity 464.625 mg/g against PSMPS adsorption. The enhancement could be related to the formed n–n heterojunction, magnetic field promoted charge separation, spin polarization, and mass transfer, which can suppress the recombination of charge carriers and extend the photoresponsive range. The PS adsorption process followed a pseudo first order kinetics and fitted well with the Langmuir isotherm model. The AMX photodegradation also followed pseudo-first-order kinetics, with a rate constant of 0.0220 min^{-1}. After exposing g-C_3N_4/Fe_3O_4 to 0.5T magnetic field in 150W UV light, the rate constant increased to 0.02368 min^{-1}. These findings highlight the potential of magneto-enhanced Fe_3O_4/g-C_3N_4 NSs as multifunctional catalysts for the effective removal of antibiotic and microplastic pollutants from water systems.

***Key words**: Adsorption, Amoxicillin, Microplastics, Magnetic field, g-C_3N_4/Fe_3O_4, photocatalysis, polystyrene*

Chapter 1

Introduction

1.1 background of the study

The emerging contaminants of wide international concern include four major categories: antibiotics, microplastics, endocrine-disrupting chemicals, and persistent organic pollutant (Pei et al., 2025). Microplastics (MPs) and antibiotics (ATs), two significant categories of pollutants of expanding concern, coexist in aquatic habitats, and their interactions are a growing cause for concern (Y. Wang et al., 2021). MPs have recently emerged as a worldwide pollutant of concern. They are defined as plastics at the micron scale (usually, plastic materials smaller than 5 mm).

After exposure to sunlight, biological degradation, and mechanical abrasion, the discarded plastic waste breaks down, embrittles, and fragments form MPs (C. Wang et al., 2021). MPs, are the major environmental issue since the excessive usage of plastic products has resulted in an approximated 4.8–12.7 million tons of pollutant entering the ocean from land each year (Indhur et al., 2025; Wang et al., 2024). Plant growth, nutrient absorption, and root-shoot development are all hindered by MPs. They harm kidneys, inflame the gastrointestinal tract, and disrupt reproduction in aquatic species. Since humans are the top consumers in the food chain, they are at risk because MPs can harm their immune systems, stress reactions, and reproductive and developmental health (Giri et al., 2024).

Nowadays, the technologies that are practical for removing microplastic from water include physical, chemical, and biological methods. Chemical treatment procedures like photocatalytic oxidation and oxidation removal can completely remove MPs in body of water, but they have the disadvantage of being costly and energy-intensive. Biological treatment typically takes a long time despite being regarded as a promising technology (Shi et al., 2022). Wastewater treatment plants play a key role in reducing pollution but are not yet designed/optimized to effectively remove microplastics, highlighting a critical gap to address (Indhur et al., 2025). In these days, the use of magnetism enhanced adsorption separation was reported in assay of MPs in water. The hydrophobic surface of MPs can be magnetized via binding nanoparticles (Grbic et al., 2019)

Antibiotics are also the useful medicine that enhances the health of both humans and animals, and they are commonly used in aquaculture and medicine. The semi-synthetic β-lactam amoxicillin (AMX) is frequently utilized to cure bacterial infections and other illnesses. According to reports, between 30 and 90 percent of AMX released into the environment through animal and human waste (Ma et al., 2023). AMX remains in aquatic bodies may have a adverse effects such as Harmful towards microalgae and different species, short-term, long-term health impacts, and deterioration of the environment. While pharmaceutical industry levels can exceed mg/L, AB resistance can form at µg/L level. Amoxicillin residues must be effectively removed to avoid negative effects because they are chemically resistant and dangerous even in trace levels. Currently, adsorption, chemical oxidation, microbial degradation, and other processes are used to remove (Wahyuni et al., 2024).

Magnetic force enhanced photocatalysis has recently attracted a lot of interest as one of the most promising methods for degrading these antibiotic pollutants since it is inexpensive, effective, and environmentally friendly while breaking down antibiotics in ambient light and sunshine. Since the majority of antibiotics have strong molecular structures that prevent them from breaking down, it is critically necessary to finding, design, and fabricate suitable photocatalysts with high photocatalytic activity (Bian et al., 2021) (Bai et al., 2022).

Graphitic carbon nitride (g-C_3N_4) is from the many photocatalysts that attracted a lot of interest because of its special qualities, which include a reasonable band gap, outstanding chemical stability, large specific surface area, and non-toxicity (Li et al., 2023). Furthermore, the primary functional groups in g-C_3N_4 are -NH_2, -NH-, or =N- act as an adsorbent by interacting with microplastics through complexation or chemical reactions, removing them from the aqueous environment. However, the low light absorption capacity and quick recombination of photoproduced charge carriers frequently restrict C_3N_4's photocatalytic effectiveness (Duan et al., 2019).

The creation of heterostructures through the coupling of g-C_3N_4 with different catalyst material has been extensively investigated as a means of getting around these restrictions. Magnetite Fe_3O_4 is an attractive candidate in this investigation because of its great magnetic and visible light absorption capabilities (Li et al., 2023)

Even though Photocatalysis and adsorption have attracted much interest, they still require further efficiency improvement due to environmental pollutant management challenges. Although surface modification, heterojunctions, and doping can increase photocatalytic and adsorption efficiency (Sun et al., 2024). They are frequently associated with high costs, environmental toxicity, and restricted sustainability. The external magnetic field-assisted approach has drawn more attention recently and is thought to be a successful approach to boost photocatalytic activity. because of its simple introductions and controllable conditions (Sun et al., 2024). It improves charge separation and, therefore, reduces electron-hole recombination. Magnetic photocatalyst particles are aligned for better surface exposure and interaction with pollutants. This method of enhancement is controllable, reversible, and non-invasive compared to permanent chemical modifications, thus not affecting the intrinsic properties of the material. Besides, it makes the recoverability and reusability of magnetic photocatalysts easier. It is an environmentally friendly and sustainable enhancement technique (Gao et al., 2019). Even though magnetic fields offer a noticeable advantage, there is a limitation of studies integrating them with photocatalysis and adsorption.

1.2 Statements of the problem

Mass production and limited recycling of plastics have led to large amounts entering aquatic environments, where they break down into microplastics. Polystyrene (PS) microplastics, due to their small size, are easily ingested, migrate with the food chain, and stay in the ecosystem since they prevent Biological degradation and photocaltysis making them nearly impossible to remove once released. These properties pose serious dangers for both humans as well as the surroundings. The development of antibiotic-resistant bacteria and genes that accelerates the development of antibiotic resistance and endangers both natural systems and human health. Because of the potential impact to human health as well as the environmental harm, antibiotic pollutants are considered to be one of the most environmental issues facing the globe in the twenty-first century (Bai et al., 2022).

Therefore, it is crucial to develop efficient methods for removing microplastics and antibiotics, as current technologies face limitations in efficiency, cost, toxicity, and environmental impact. The complex nature of these pollutants further underscores the need for sustainable solutions. Therefore, this research focus to address the gap via focusing the use of magneto-enhanced g-C_3N_4/Fe_3O_4 nanostructures for both removals of microplastics and antibiotics, particularly by using the synergetic effects of magnetic field integration on both photocatalysis and adsorption.

1.3 Objectives of the study

1.3.1 General objectives

The main aim of this study is to synthesize, characterize and magnetically enhance g-C_3N_4/Fe_3O_4 nanostructure for photocatalytic amoxicillin degradation and polystyrene microplastic adsorption from water samples.

1.3.2 Specific objectives

- To synthesize g-C_3N_4/Fe_3O_4 nanostructure via coprecipitation method.
- To characterize the structural, crystal, optical, and morphological properties of the synthesized g-C_3N_4/Fe_3O_4 nanostructure.
- To optimize the pH, pollutant concentration, duration of time and catalyst amount during photocatalysis and adsorption process.
- To evaluate the efficiency, magnetic recoverability and reusability of the prepared composite

1.4 Significance of the study

The photocatalytic degradation of antibiotics works to reduce the spread of antibiotic-resistant bacteria and address the environmental consequences of pharmaceutical contaminants. At the same time, the magneto responsive adsorption-based removal of microplastics goes a long way in solving a problem that has gained global prominence by providing a technique to trap and remove rattling contaminants from water bodies.

The research further investigates the basic principles behind the adsorption and photocatalytic processes. The work makes clear contributions to understanding the mechanisms by examining the role of magnetic properties on these mechanisms which should enhance the ability to develop more effective and practical solutions. Moreover, applying magnetic fields to improve photocatalytic activity is a promising approach that could change the dynamics of contaminant removal technologies. The study will generally have the following significance

- The magnetic features of the composite improve separation, recycling, and reusability for sustainable water treatment.

- It studies the adsorption and photocatalysis phenomena, which is aimed at pollutant removal and gives a mechanistic understanding of the process.
- Cost-effective and industrially usable environmental remediation technologies are developed as a result of the study.

1.5 Scope of the study

This research explores the development of magneto-enhanced C_3N_4/Fe_3O_4 composites as a multifunctional material for dual applications in environmental remediation, focusing on the photocatalytic degradation of antibiotics and the photo responsive adsorption-based removal of microplastics. The research includes a detailed investigation such as material synthesis protocol, the crystal, morphlogcal, optical and electrochemical properties, adsorption kinetics, isotherm, and photocatalytic properties of the magnetic nanoparticles (MNPs) to understand their efficiency and mechanisms. In addition, the magnetic properties were also be used in the material's reusability and recovery potential. However, this study does not include the long-term environmental impact assessment of the degraded products, large-scale device fabrication

Chapter 2

Review of related literature

2.1 A review of micropatics and Antibiotics Water Pollution Challenges

The need for fresh water is rising in many regions of the world due to crowded, growing cities, irrigation growing, use of different plastics, fast production of antibiotics, and planners are unsure of how to meet the water demands of the future. MPs are one of the primary sources of water contamination. An estimated 70% of the more than 9 billion tons of plastic products created since their commercial launch were thrown away, leaving behind roughly 7 billion tons of plastic garbage in total (Capodaglio, 2025). However, particularly in developing country, plastic garbage is frequently mis-handled and disposed of in surface waters, uncontrolled landfills, or the ocean. Plants that accumulate microplastic are known to exhibit reduced growth, absorption, and suppression of shoot and root development. When aquatic animals consume microplastics, they may develop kidney damage, gastrointestinal tract inflammation, and reproductive organ abnormalities, among other effect. Humans, the largest consumer in all food chains, are particularly susceptible to microplastics since they consume aquatic foods. Microplastics have been shown to impact immunological and stress responses in humans, as well as cause toxicity to the reproductive and developmental system (Giri et al., 2024)

The presence of antibiotic residues in surface waters affects the microbial communities' compositions and functions. Surface water-dissolved antibiotics can reach sub-inhibitory quantities that impact microbial ecology by accelerating the rate of mutation, transferring drug resistance genes horizontally, and boosting the growth of bacteria resistant to antibiotics (Ma, 2025). Drug-resistant bacteria (DRB) as well as drug-resistant genes (DRGs) are becoming more common in the environment due to the extensive use of antibiotics worldwide, which has increased selected pressures. This is made worse by Forward shift of genes by Movable genetic components. Antimicrobial refusal (AMR) is a proposed rising global pollution issue that poses a hazard to human health since, if unchecked, it could result in 10 million deaths annually worldwide by 2050 (Ma, 2025).

As the world's water crisis increases, a major public survey indicated that water pollution is the most pressing environmental issue for people worldwide, more than even climate change. Additionally, there is a growing desire for initiatives to address water challenges, such as putting more of an emphasis on freshwater ecosystem restoration and protection and on companies working together (Grafton et al., 2025).

2.2 Photocatalysis for Water Treatment

Photocatalysis is a method that employs light and a semiconducting material as a catalyst. It is a process occurs when a semiconducting substance is exposed to light, creating an electron-hole pair. The negative ion (e^-) and positive hole (h^+) pairs have oxidation and reduction ability. Photocatalysis is now recognized as a new or alternative technology that complements the existing water treatment process. (Fang et al., 2020).There are several advantages of photocatalytic environmental remediation such as low-cost, efficient method that uses harmless semiconductors to transform environmental pollutants into light with the right wavelengths. There are three main processes involved in photocatalytic remediation of the environment; photon absorption, excitation, and reaction (Ma et al., 2024).

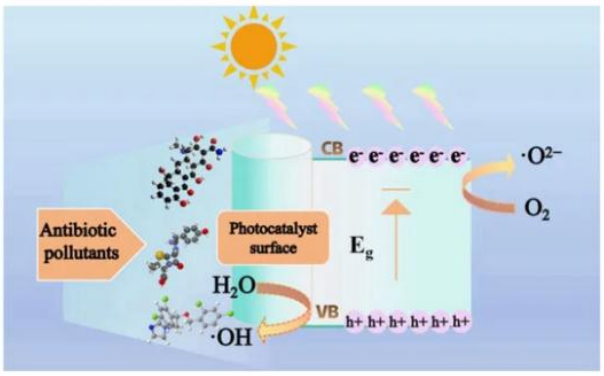

Figure 2. 1 The process by which antibiotics undergo catalytic oxidation

2.2.1 Semiconductor Photocatalysts

Photocatalytic semiconductors are important for pollutant removing from environment. Still, number of limitations that decrease the effectiveness of photocatalytic semiconductors. For instance, when exposed to visible light, single-phase semiconductor energy band gaps are inactive. The visible light can be absorbed by semiconductors with a narrower band gap, and ultraviolet (UV) radiation can be

absorbed by semiconductors with a wider band gap. About 45% of light is made up of visible light, while the remaining 5% is made up of UV rays (Alahmadi, 2022).

2.2.2 Overview of g-C_3N_4 as a catalyst

Graphitic carbon nitride (g-C_3N_4) is one of the many photocatalysts that has attracted a lot of interest because of its special qualities, which include a reasonable band gap, outstanding stability, as well as non-toxicity. However, the low light absorption capacity and quick recombination of photoproduced charge carriers frequently restrict g-C_3N_4's photocatalytic effectiveness. The creation of heterostructures through the coupling of C_3N_4 with other catalyst has been extensively investigated as a means of getting around these restrictions (Bai et al., 2022). Different studies showed that the morphology of g-C_3N_4 NSs plays a main role in boosting the photocatalysis activity.

Some 2D materials with outstanding characteristics, such graphitic carbon nitrides (C_3N_4), were widely employed recently for a variety of application, such as remediation of the environment, chemical sensors, electronic and optical devices, and energy generation and storage (Wudil et al., 2023).

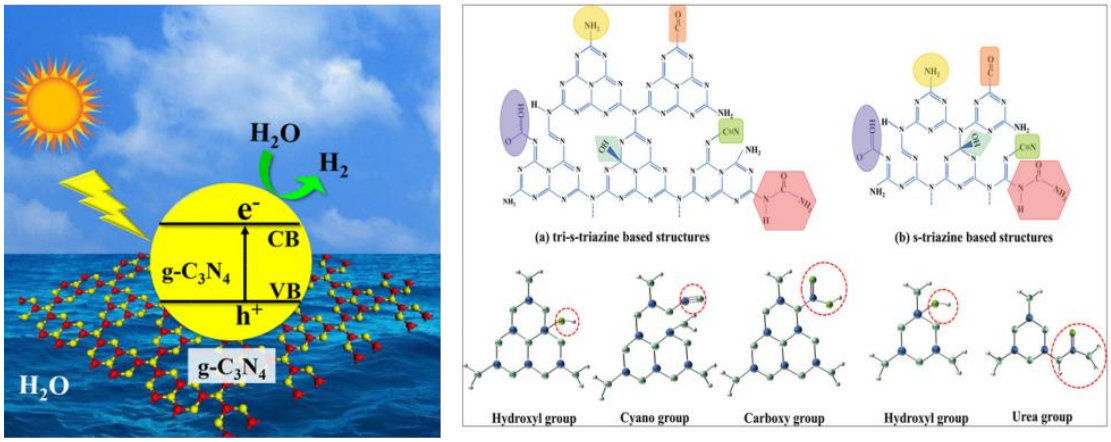

Figure 2. 2 g-C_3N_4 polymerized arrangement(Wudil et al., 2023)

Several strategies have been investigated studied so far, including morphological modulation, defect engineering, and the design and development of heterogeneous structures. The creation of heterostructures through the coupling of g-C_3N_4 with other semiconductors has been extensively investigated as a means of getting around these restrictions (Li et al., 2023).

2.3 Photocatalytic Efficiency Enhancement methods of g-C_3N_4 heterojunctions

2.3.1 Construction of metal oxide/ g-C_3N_4 Heterojunctions

The use of CN in photocatalytic activity has been limited by its wide band energy, which suggests a low absorption of solar light, its high rate of light-induced charge recombination, and its incapacity to create reactive species via photogenerated holes (h^+) and hydroxyl radicals ($OH^{\cdot}$). The assembly of bare CN with metal oxides is one of the most important strategies used to expressively overcome these obstacles and boost the effectiveness of CN photocatalysis (Nejat, 2024).

Heterojunctions between g-C_3N_4 and suitable semiconductors are now being utilized extensively to increase the efficiency of photocatalytic degradation and have been shown to be successful in increasing the efficiency of photogenerated charge separation. According to (Liang et al., 2025), the synthesized CN/Cu_2O type II heterojunction hybrid material dramatically increased its photocatalytic activity toward the production of hydrogen.While the holes migrate to the semiconductor with a more negative HOMO (Cu_2O), the electrons flow into the semiconductor with a more positive LUMO (g-C_3N_4) due to their spatial separation.

Intimate inter facial contact Sn/oxide g-C_3N_4 composites were created using an easily understood electrostatic self-assembly technique and a chemical reduction process. Three key processes contribute to the production process: mild hydrothermal preparation of oxide g-C_3N_4; electrostatic attraction-based Sn^{+2} attraction on the g-C_3N_4 surface; and chemical reduction to convert the deposited Sn^{+2} to metallic Sn metal (Zulfiqar et al., 2024). Furthermore, under visible light, the resulting metallic Sn-attached oxide g-C_3N_4 NCs show excellent stability and a significantly increased catalytic activity for the removal of MO and phenol (Zulfiqar et al., 2024).

2.3.2 Applying magnetic force

Recently, the external-fields-enhanced photocatalytic efficiency has taken great interest. A photocatalyst with magnetic characteristics is used in (PMC) degradation, usually by combining photocatalytic materials like zinc oxide (ZnO) and titanium dioxide (TiO_2) with magnetic materials like iron oxide. This combination makes it

simple to recover and reuse the catalyst by allowing it to be readily removed from the pollutant complex utilizing magnetic (Nugroho et al., 2025).

An further advantageous strategy to improve photocatalytic performance is the use of various external fields to the catalytic reaction system (Dhanalakshmi et al., 2023). Specifically, it has been shown that the externally supplied magnetic field speeds up chemical processes during photocatalysis. In photocatalysts, the main separation of charge carriers is facilitated by the Lorentz force produced by the applied magnetic fields. In the MF reaction system, the catalyst carriers are oriented in the direction of the magnetic field, exposes more active sites for the removal of contaminants. Additionally, both catalysts and pollutants will be affected by the Lorentz force, this may raise the attraction between active sites with pollutants.. But instead of a non-directional transfer channel, this MF catalytic system requires a directed one, which lengthens the charge transfer path (Dhanalakshmi et al., 2023).

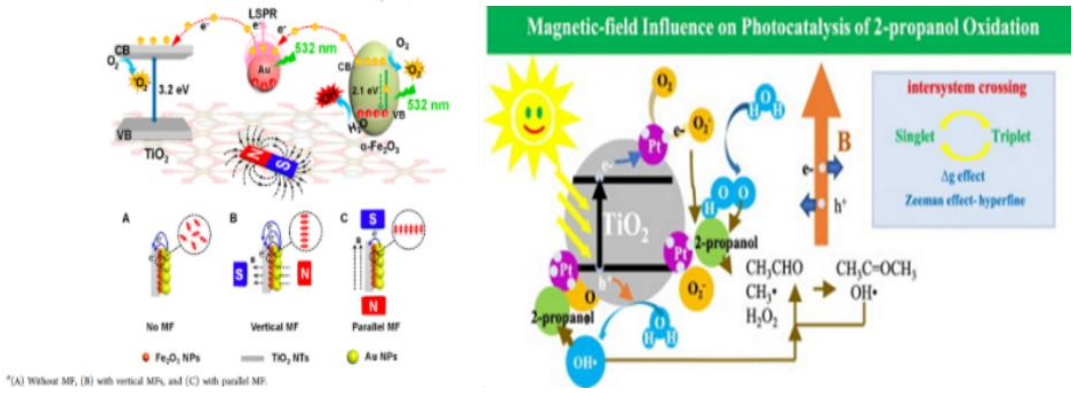

Figure 2. 3 Changing semiconductor' photocatalytic performance

The key concepts of external magnetic field supported photocatalysis are presented, along with an explanation of the mechanism of magnetic field enhanced photocatalysis from three perspectives: spin orientation, Lorentz force, and magnetoresistance action.

2.3.3.1 Lorentz force

The force exerted on a moving charge in a magnetic field is known as the Lorentz force, and it is defined as follows (Meng et al., 2023):

$$\vec{F} = q(\vec{V} \times \vec{B}) \qquad 2.1$$

q represent; the particle charge, $\vec{V}$ is the particle speed, and $\vec{B}$ is the magnetic induction strength.

The Fe-Cu bi metal enhanced modified graphene oxide (FeCu/rGO) is used to study the catalytic performance of the photo-Fenton process with or without a field of magnets (Dan et al., 2021). The photocurrent intensity of FeCu/rGO is clearly increased by a magnetic field, indicating that the Lorentz force generated by the magnetic field can effectively promote the distinguishing of photogenerated electrons and holes (Dan et al., 2021)

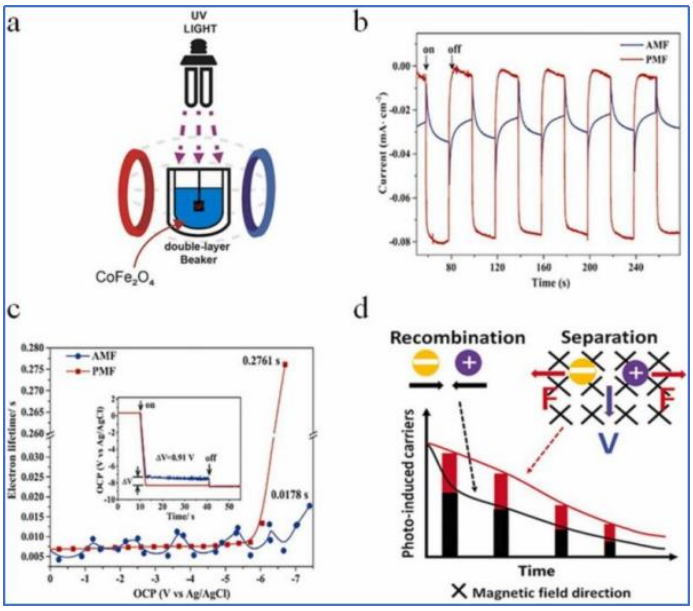

Figure 2. 4 (a) A diagram showing the heterogeneous photocatalysis system when a magnetic field is present (b) dynamic curves of light current with time and (c) electron lifetime as a function of Fe_5Cu_5/rGO's open-circuit potential (d) A schematic representation of the suggested impact of the magnetic field on the separation of photoinduced charge carriers in the TiO_2 nanobelts

For example as (Bian *et al.*) shown, the magnetic force increase the photocatalytic degradation of methyl orange by commercial TiO_2 powder by 24%.

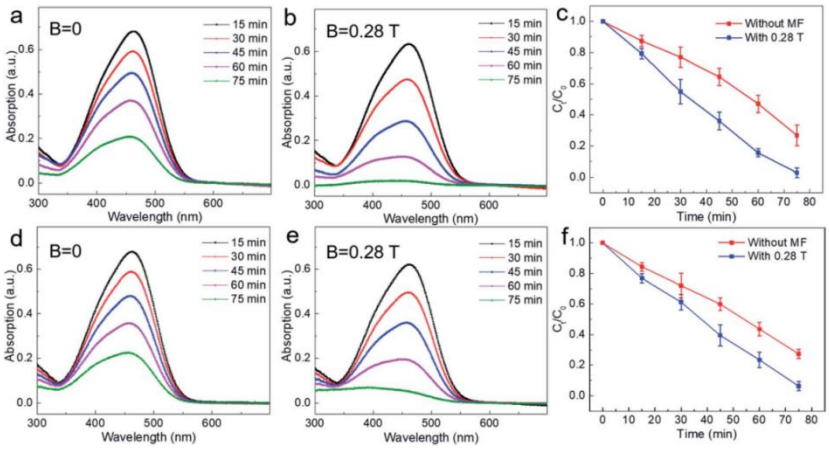

Figure 2.5 The conditions (a) without a magnetic field and (b) with a modest magnetic field of B ¼ 0.28 T. (c) the ¼ 0.28 T magnetic field and its effect on the degradation rate over time. (d) presence and absence magnetic field (e) in presence of B ¼ 0.28 T for the 48-hour settling condition, respectively (f) Degradation rate variation over time with and without a magnetic induction B ¼ 0.28 T (Test results error bars have been acquired by performing the test 3* under similar lab circumstances). (Bian et al.).

2.3.3.2 Magnetoresistance effect

One significant spintronic phenomena is the magnetoresistance effect, which is the Change in opposition of certain materials if a magnetic field is exerted.

$$R(\%) = \frac{Rh\text{-}Ro}{Ro} \qquad 2.2$$

where the magnetoresistance effect's magnitude is denoted by R (%); Ro, RH represent the resistance of the material when the magnetic induction is o and H, rThe phenomenon known as the "positive magnetoresistance effect," mostly present in magnetic materials, occurs when a material's resistance rises as the magnetic field does. The inverse magnetoresistance influence modifies the charges's spin orientation and influences its transport behavior. This significantly increases the photocatalytic efficiency by enabling additional photoproduced carriers of charges to arrive at the target site.

(Li et al., 2018) described how α-Fe_2O_3/modified GO hybrid nanostructures (Fe_2O_3/RGO) performed photocatalytically with a magnetic, significantly increasing the photoproduced electron carrier transfer performance by the use of the negative magneto-resistance influence (Fig. 3a).

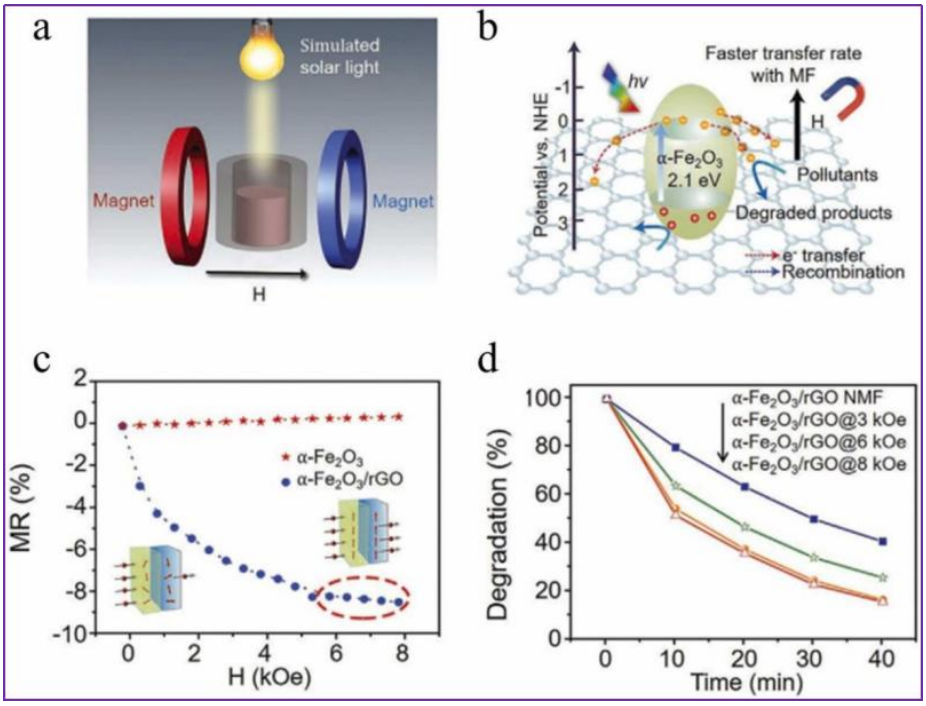

Figure 2.6 (a) graphical explanation of the magnetic photocatalysis device, (b) pictorial representation of the suggested photocatalytic process in the magnetically field-induced α-Fe_2O_3/rGO composites, (c) magnetotransport characteristics of a-Fe_2O_3 and α-Fe_2O_3/RGO nanocomposites at room temperature, and (d) light assisted of RhB with various magnetic fields in the presence of α-Fe_2O_3/rGO hybrid nanostructures under Xe light irradiation.

2.3.3.3 Spin polarization

Spin orrientation is the degree to which spin orientations are aligned with a specific direction, while spin is the intrinsic angular momentum of electrons. There are two spin arrangements for electrons: spinup and spindown (Liu & Mao, 2025). The electron's spin orientation will change when a small amount of energy is added to the reaction; this change in spin state will impact the catalytic process. Spin transferring is impossible if the electrons' spin-up and spin-down states are equally distributed.

Therefore, in solid catalysts, net spin generation is needed. Spin polarization has been shown to improve photocatalytic performance. According to the Pauli exclusion principle, an excited electron in the conduction band can only be taken by holes if the holes' spin orientations differ from those of the stimulated electrons (Liu & Mao, 2025).

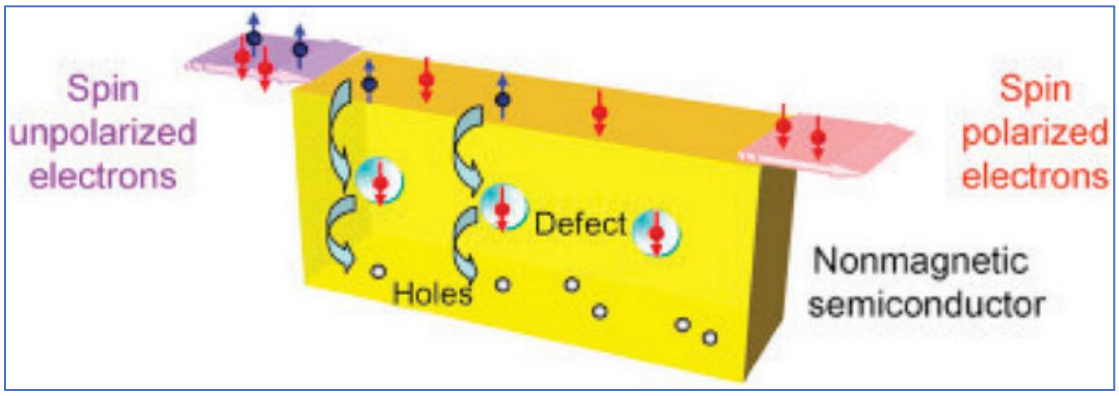

Figure 2.7 Schematic of electron capture and recombination in the presence of spin polarization

2.4 Degradation path of amoxicillin (AMX)

Hydrolysis and photolysis are the primary processes by which amoxicillin (AMX) degrades, producing less stable and potentially bioactive byproducts which could persistence in the environment. Under UV-Vis irradiation for 300 hours, TiO_2 anatase was able to degrade AMX almost completely. In the presence of light, the AMX attracted with the mineral and broke down into simpler compounds, as shown in Figure 2.7a. The suggested breakdown of AMX into various compounds in the absence of minerals under dark and sun radiation is depicted in Figure 2.7b (Ali & Maafa, 2024).

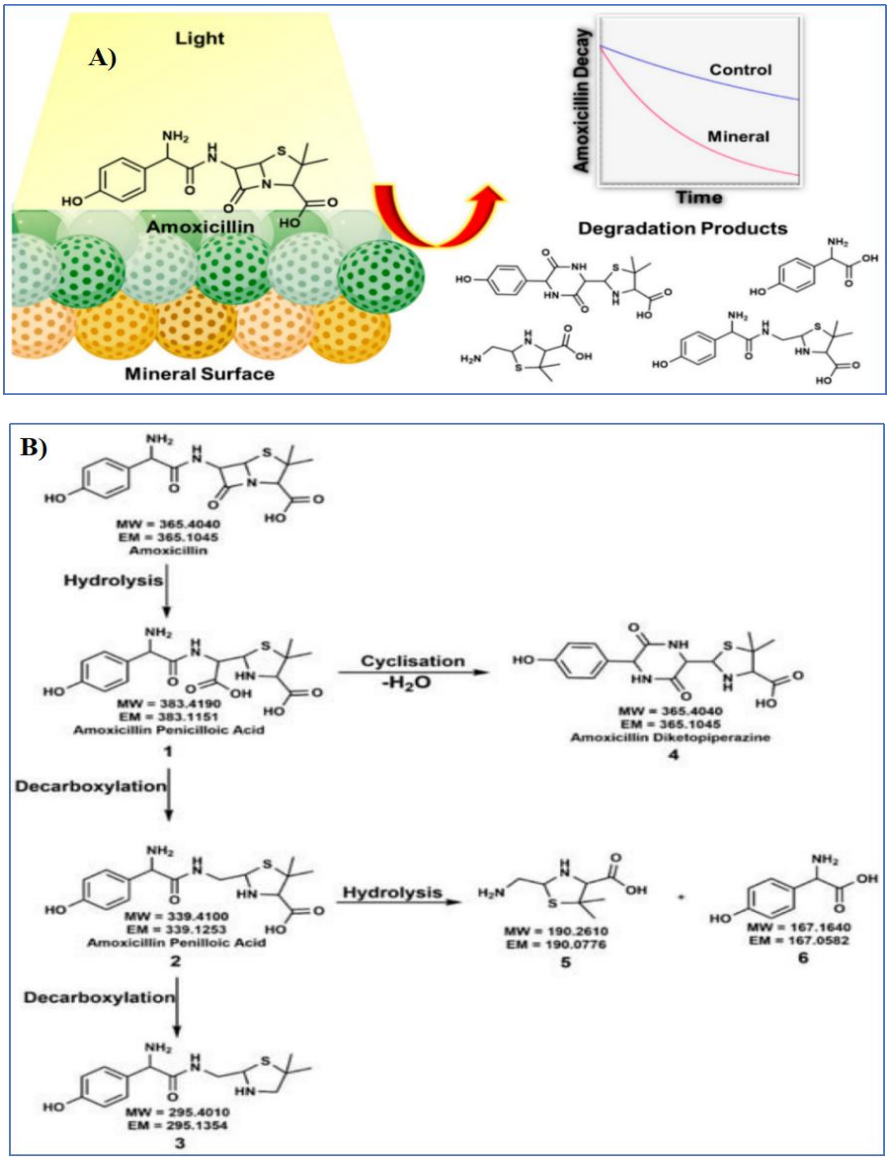

Figure 2. 8 a) AMX-mineral interaction and b) degradation pathway

2.5 Adsorption of Microplastics

Because of their tiny size, enormous area of surface, and great hydrophobicity, MPs can easily absorb a variety of hydrophobic organic contaminants, heavy metals, and pathogens, which can have a major negative impact on the ecosystem itself. adsorption is a commonly used technique for the elimination of pollutants in water environment, which is deepened on the interaction of a material called an adsorbate with an adsorbent material's surface at the two phases' contact (García-Rollán et al., 2025).

Both physio-adsorption and chemisorption adsorption are considered into consideration, depending on the kind of interactions that is formed between the adsorbent and the adsorbate. Weak forces including dipole-dipole, hydrogen-based, van der Waals, and electrostatic forces are a few examples that are responsible for physical adsorption. This process has modest enthalpy values and is reversible. On the adsorbent surface, the attracted substances or particles in this instance have some mobility. In contrast, chemical adsorption has a substantially greater enthalpy than physical adsorption because the adsorbate ways a chemical bond with the sorbent surface, rendering the association irreversible (García-Rollán et al., 2025).

The extensive usage of plastic polymers, which are regularly found in wastewater treatment facilities, has made polystyrene (PS) one of the most important MP kinds. Additionally, PS has special qualities that allow it to enter aquatic habitats and wastewater treatment, including a slow rate of biodegradation and buoyancy and light weight.

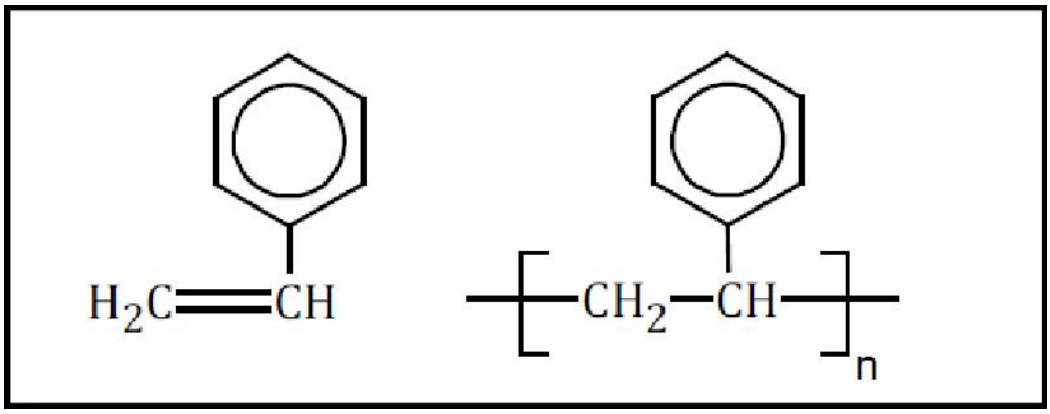

Schem 1. Structure of styrene and polystyrene

Therefore, as shown in Schem 2, the strong interfacial bonding and π-π interaction between PS MPs and the Ni/rGO nanocomposite may be responsible for their adsorption. Furthermore, rGO's hydrophobic properties which come from the presence of sp2 hybridized carbon atoms help it interact with the hydrophobic organic molecules of polystyrene microspheres, which causes aggregates to form by van der Waals forces (Karunattu Sajan et al., 2024).

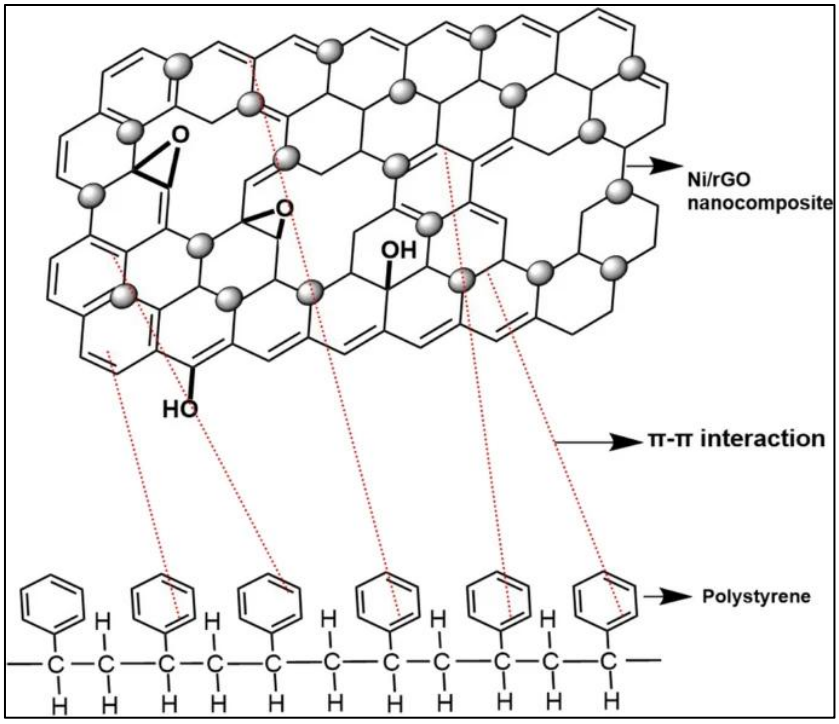

schem 2. Adsorption PS on Ni/rGO

2.6 Ways and application of magnetic field boosting pollutant adsorption

The application of an external non-contact force enhancing Adsorption is a versatile and manageable techniques. Addition of magnetic forces to adsorption may change the properties of the bulk mixture, adsorbent, and adsorbate, this increase adsorption performance. Magnetic fields in several ways were employed to investigate the study of the magnetic force on the adsorption process (Ding et al., 2025). These include magnetostatic and time-changing magnetic fields, that have varied degrees of effect on pollutant adsorption. Absorbents are the most important components of the adsorption mechanisms. MNPs have a large specific surface area, are easily functionalized, environmentally friendly, and magnetically sensitive, making them ideal adsorbents (Ding et al., 2025)

According to (Lo et al., 2021) the degree of aggregation and to improve the efficiency of adsorption. In comparison to pure nano-magnetites (15.3 ± 0.6%), the study shows the removal efficiency of Cu^{2+} ions on the nanomagnetite silicagel composite has enhanced by 22.4%. Before adsorption, the NMSG is exposed to a magnetic field, which reduces the adsorption capacity by 39% (from 11.2 ± 1.1 to 15.6 ± 1.6 mg/g). It deduced that an enhanced Lorentz Field during attraction was the consequence on the

Magnetic force aligning the magnetic domains inside the nano-magnetites. Because of extreme aggregation, such orientation of magnetic coils is almost unachievable in pure nano magnetites. We also discovered that by altering the field's strength and configuration, an external MF may be used to control the NMSG's adsorption capacity (Lo et al., 2021).

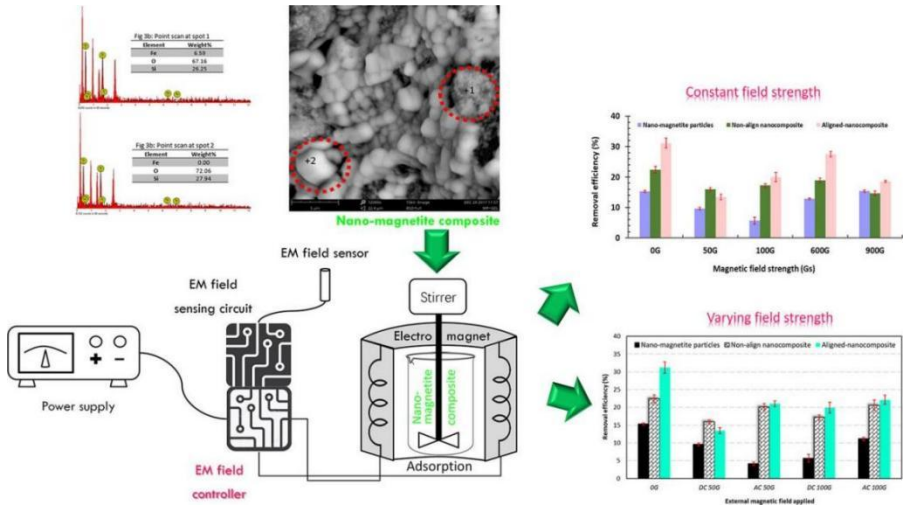

Figure 2. 9 Influence of external magnet force on adsorption

Coppre(II) and CIPs were selected as the sample pollutants by, which demonstrates a considerable 24.2% enhancement of CIP's adsorption strength. The attraction speed of CIP and Copper(II) are significantly increased by 359.76% and 371%, respectively, although the magnetic influence of the adsorption capacity of Cu^{2+} is not evident, indicating the selectivity for adsorption. The main thing to determining the adsorption increase using a (RMF) is to promote the kinetics of material transfer, alter the hydrogen bond, and measure the reactivity of surface reacting molecules. The adsorption process and the selectivity of contaminants may be modified by combining the external magnetic field with the adsorbent's intrinsic magnetic characteristics. Additionally, it offers MF an innovative and useful way to remove pollutants in water environment (Ren et al., 2021).

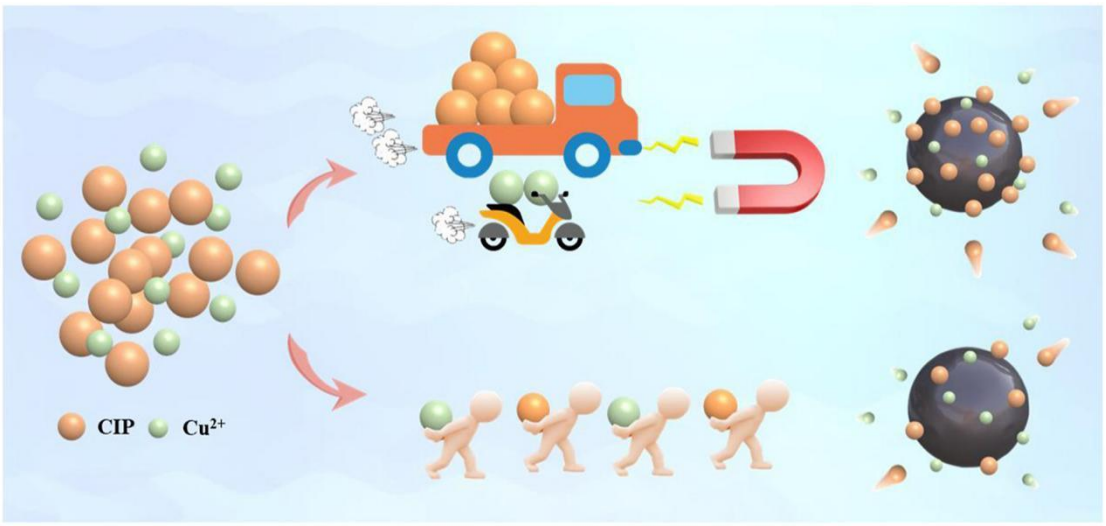

Figure 2.10 ways of magnetic force enhance adsorption

However, each ion's magnetic characteristics are crucial, and the ions' sensitivity to the magnetic field is correlated with each ionic species' magnetic susceptibility (an attribute that is inherent to every element). Both the sign and the magnitude of the magnetic susceptibility value are significant (González Vázquez et al., 2020). As a result, a higher value for this component means that it is magnetized in a way that is favorable to the applied magnetic force (para-magnetic or ferro-magnetic), while a negative value means that the applied magnetic field is repelling it (diamagnetic). A diamagnetic adsorbate was discovered to have a higher adsorption capability in earlier research.

In addition, since water is diamagnetic and is magnetically susceptible of its own, the molecules which are affixed to the ion also exert a exerting force. Thus, the following formula is used to determine the hydrated ion's magnetic susceptibility (González Vázquez et al., 2020), χ_h :

$$x_h = x_{mag\ ion} + [(n_h)(\chi_{H2O})] \qquad 2.3$$

Where, X_{H2O} is the magnet permeability of the liquid, nh is the solvation amount, and χmag ion is the ion's magnetic permeability.

Chapter 3

3. Methodology

3.1. Study Location Description

Synthesis of CN, Fe_3O_4 and CN/Fe_3O_4 nanostructure was conducted at the Postgraduate laboratory of Adama Science and Technology University (ASTU), Department of Applied chemistry. The XRD, UV-DRS characterization and PS adsorption was experiment was conducted at ASTU, Department of Material Science and Engineering. The FTIR characterization was done at Addis Ababa Science and Technology University. SEM, FE-SEM, SEM-EDX, XPS, and BET characterizations were done at Chungnam National University, South Korea. The electrochemical experiment was conducted at the electroanalytical laboratory of ASTU, Department of Applied Chemistry. The photocatalytic experiments were also done at wollega university.

3.2. Chemicals and Reagents

Urea, Iron (III) chloride hexahydrate ($FeCl_3 \cdot 6H_2O$, >95%) and iron (II) chloride tetrahydrate ($FeCl_2 \cdot 4H_2O$, >95% purity), ammonium hydroxide (NH_4OH, 25% aqueous solution), pharmaceutical-grade amoxicillin (AMX) obtained from Adama Health Research and Referral Lab group (APHRRLC), polystyrene (PS) powder[CAS#25704-18-1]. FTO (resistivity 4.01×10^{-4} Ω.cm), sodium hydroxide (NaOH) pellets, Na_2SO_4 (99%), KCl (99.95%), Ethanol (99.9%), all chemicals were purchased from Sigma-Aldrich; and distilled water(distiller, LB-12EWD) obtained from ASTU at Department of Applied Chemistry; were used in this work. All chemicals were used without any further purification.

3.3 Synthesis of g-C_3N_4, Fe_3O_4 and g-C_3N_4/Fe_3O_4 MNPs

3.3.1 Synthesis 2D g-C_3N_4 nanosheets

The g-C_3N_4 nanosheet has been synthesized according to (Li et al., 2023) with little a modification. Initially, 15 gram of urea were putted on a semi-closed crucible and warmed in a muffle furnace at 550°C for four h and the temperature change rate maintained at 2 °C per minute. After the thermal treatment, the resulting yellow powders were allowed to cool naturally to room temperature. The cooled product

were rinsed thoroughly with distilled water and ethanol and dried at 60 °C for 12 h. Following the drying process,The results were heated at a rate of 5 °C per minute for 330 minutes at 500 °C in a muffle furnace for a second round of calcination.

3.3.2 Synthesis of Magnetite (Fe_3O_4)

Magnetite NPs were synthesized by co-precipitating methode Fe^{3+} and Fe^{2+} ions (molar ratio 2:1) in a basic solutions. $FeCl_3{\cdot}6H_2O$ (3 g) and $FeCl_2{\cdot}4H_2O$ (1.104 g) were dissolved in 100 mL deionized water and maintained at 90 °C for 10 minutes with continuous magnetic stirring. Then, NH_4OH (10 mL) was added dropwise and separated using an external magnet (Appendix figure 1a). To remove impurities, the obtained Fe_3O_4 MNPs were rinsed three times with distilled water and ethanol. They were then dried in an oven at 60 °C for 12 h.

3.3.3 Synthesis of g-C_3N_4/Fe_3O_4 magnetic nanostructures

The CN/Fe_3O_4 magnetic nanostructures (MNSs) were prepared according to (Yang et al., 2016) with minor modifications. g-C_3N_4 (1 g) was added to a solution of ethanol-water (180 mL, volume ratio 1:2) and sonicated for 3h at ambient temperature. $FeCl_3{\cdot}H_2O$ (0.919 g) and $FeCl_2{\cdot}H_2O$ (0.3515 g) were dissolved in 50 mL of water and mixed with the CN solution. The resulting mixture was agitated for 10 minutes at 90 degrees Celsius. The mixture was then treated with 10 milliliters of ammonia (25% NH_4OH). After shaking for another 30 minutes, the mixture was left to cool naturally.The synthesized g-C_3N_4/Fe_3O_4 NSs were separated from the solution using a magnet and cleaned repeatedly with ethanol and water. Lastly, the Magnetic nanocomposites were dried at overnight. For purposes of contrasting, different mass amounts (40%, 50%, and 60 weight percent) of Fe_3O_4 were synthesized in nanostructures photo-catalysts and tagged, Gf40, Gf50, and Gf60, respectively.

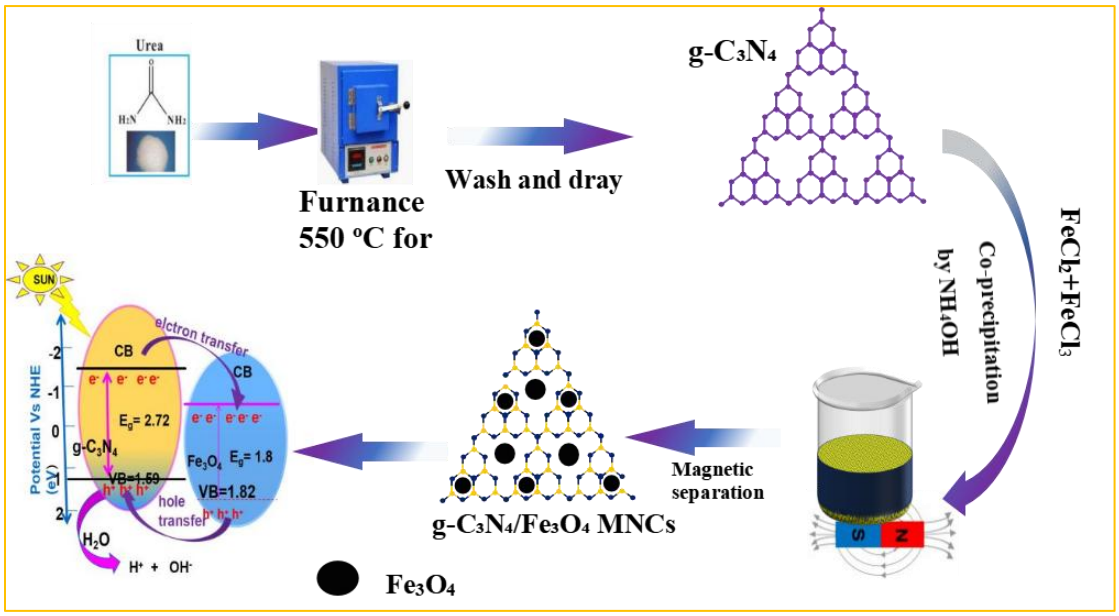

Figure 3.1 Synthesis of 2D g-C_3N_4/Fe_3O_4 MNS, g-C_3N_4 and Fe_3O_4

3.4 Material Characterization

The analyses of crystalline phases were performed by X-ray diffraction (XRD) using XRD-7000 X-RAY DIFFRACTOMETER, SHIMADZU Corporation (Japan) with CuKα (λ = 1.542 Å) radiation, a 2θ range of 10–80°, and a step size of 0.02°. The morphologies of the materials were analyzed using SEM equipped with energy disperse spectroscopy (EDS) for the analysis of the surface elemental composition. The elemental composition and oxidation states of synthesized materials were identified using X-ray photoelectron (XPS), The surface area and porosity of synthesized magnetic responsive g-C_3N_4/Fe_3O_4 were analyzed using (ASAP 2420 V2.09 (V2.09 J) BET instrument. FTIR spectra of g-C_3N_4, Fe_3O_4 , and g-C_3N_4/Fe_3O_4 were determined using a (IS50 ABX Thermoscientific , USA) and were measured from 4000 to 400 cm^{-1}. UV-DRS were also done using (UV-3600Plus Series), with 5.0 nm Slit Width, between 220.00 and 800.00 nm range to analyze optical properties and band gap of synthesized samples. The photo-luminescence were also done with (cary Eclipse, my18510001) instruments from 350nm excitation wave wavelength.

3.6 Electrochemical Characterization

The Catalysts' flat band potentials, redox ability and charge-transfer resistance (R_{CT}) were measured using Mott–Schottky, Cyclic voltammetry (CV), and EIS in a (three-electrode system) with an IVIUMSOFT potentiostat (Ivium Technologies, Netherlands, A09084). Platinum wire used as counter electrode, a sample deposited on an FTO substrate used as the working electrode, and Ag/AgCl used as the reference electrode in the three-electrode system.

The Mottschottky analysis were performed in a 0.5 M Na_2SO_3 solution in a potential window of −1.3 to +1V, while EIS experiments were performed in an solution containing 1M KOH, beetween the frequency range of 0.1hz to100 KHz The working electrodes were fabricated by mixing 10 mg of the prepared sample in 0.1M of PVA solution, depositing 40 μL of the mixture-solution on a 1 cm^2 area of the FTO substrate, and drying it for 6 h in air. The CV experiment was also done in 1 M KOH aqueous solution between -1.2 and -0.5v potential scan.

3.6 Point of zero charge PZC analysis

The state in which a catalyst's electrical charge density is neutral is known as the PZC. The PZC for a variety of nanomaterials, such as CN, Fe_3O_4, and CN/Fe_3O_4 NSs, was determined using the salt addition technique. 50 mL of a 0.01 M NaCl aqueous solution were mixed with 0.10 g of the synthesized catalysts. Initially, 0.1M solutions of NaOH and HCl were used to adjust the pH of the solution, which ranged from 4 to 9. Then, the mixtures were stirred for a full day at ambient temperature. The samples were centrifuged after agitation, the change in pH that obtained was measured. Finally, the pH change (ΔpH) is plotted against the initial pH to identify the point where ΔpH equaled zero (Feyie et al., 2024).

3.7 PS adsorption removal studies

This procedure was performed according to (Heo et al., 2022) with slight modifications. To produce an adsorbent stock solution, 20 mg of powdered CN, Fe_3O_4, and CN/Fe_3O_4 composites were added to a glass container filled with enough deionized (DI) water to reach a concentration of 200 mg/L of CN, Fe_3O_4, and CN/Fe_3O_4 MNP.

To prepare a final PS amount of 40 mg/L, 0.15 g of CN/Fe_3O_4 and the required aliquots of the PS particle (sorbate) mix were added into a 100 mL volumetric flask containing deionized water. The concentration of 40 mg/L was chosen as it exceeds current environmentally relevant levels, thereby simulating possible future increases in plastic particle pollution and localized hotspots such as accumulation zones. The resulting suspension was then agitated on shaker at revolutions per minute (rpm),for predetermined contact times (Lu et al., 2021). Each glass was then placed on a magnet for three minutes to remove the Fe_3O_4/g-C_3N_4–PS complexes from the solution. Following this magnetic detachment, the resulting solution was added to a quartz cuvette, and the absorbance of the residual PS concentration was measured using a UV-Vis spectrophotometer set to 223.5 nm. The concentration of unseparated PS particles was determined using a curve of calibration that relates absorbance to PS particle concentration.

To check the adsorption performance of the adsorbent with applied external magnetic field, the procedure above were repeated by applying **0.5T** rotating magnetic field during adsorption procedure keeping other parameters constant. Once the adsorption is done, a magnetic field will be used to collect the adsorbent with the microplastics from the liquid. The MNPs will then be cleaned and tested for reuse across several cycles by washing with ethanol or another suitable solvent to remove the microplastics.

The equation (eqn, 3.1 and 3.2) were used to determine the removal performance (R) of the adsorbent and the adsorption capacity (Q_e) of CN/Fe_3O_4 NPs (Yuan et al., 2020)

$$\mathbf{Q_e = \frac{(Co-Ce)}{m} V} \qquad \mathbf{3.1}$$

$$\mathbf{R = \frac{(Co-Ce)}{Co}\ 100\%} \qquad \mathbf{3.2}$$

Where, V (L) is volume, m (g) is the amount of the adsorbent, C0 (mg/L) is the concentration, and Ce (mg/L) is the concentration at equilibrium. (Yuan et al., 2020).

3.7.1 Kinetics and Isotherms of adsorption process

Adsorption kinetics is frequently used to investigate the mechanism, reaction limiting step, and overall adsorption mechanisms.

Adsorption kinetics will be studied by exposing a known concentration of PS microplastics solution to the adsorbent and measuring the change in concentration at regular time intervals using UV-Vis spectrophotometry. The data will be fitted to kinetic models, such as pseudo-first-order and pseudo-second-order equations, in order to determine the rate constants and understand the adsorption mechanism. The fitting results will reveal whether the process is controlled by chemical interaction or diffusion (Cojocaru et al., 2024).

The adsorption isotherm describes the equilibrium interaction between the sorbent and the adsorbed species. Different initial PS microplastic concentrations were used to examine adsorption isothermal models in order to obtain understanding into the adsorption mechanism and properties of Fe_3O_4/CN on PS microplastics. A range of microplastic solutions was prepared at the optimum pH, with the aamount of 10, 20, 40, 60, and 80 mg/L. Additional experimental parameters were established in accordance with the circumstances specified in the 'Adsorption studies' section. We investigated and examined the Langmuir and Freundlich isotherm plots for PS microplastic adsorption on Fe_3O_4/CN.

3.8 Batch experiments for photocatalytic Activity Test

AMX antibiotic was utilized as a A hypothetical pollutant to assess the photocatalytic activity of the synthesized Fe_3O_4, CN, nanosheet and CN/Fe_3O_4 NCs samples Upon visible light illumination utilizing a 150 W hallow cathode lamp as a light source. To achieve adsorption–desorption equilibrium before irradiation, 25 mg of catalysts were added to 500 mL of AMX antibiotic (30 mg/L) solution and agitated without light for 30 minutes. After that, that resulting material was subjected to visible light in so as to initiate the photodegradation process. Also, the photocatalytic degradation performance of Fe_3O_4/CN with applying rotating homemade magnetic field (RMF), repeated as. Then the efficiency produced with and without RMF will be carefully calculated via.

$$\textbf{Percent degradation} = \frac{(Ci-Ce)}{Ci}\ 100\% \qquad 3.3$$

Where, Ci is the initial amount of the AMX (mg/L) and Ce is the final amount of AMX (mg/L) (Zulfiqar et al., 2024).

Chapter 4

Result and discussion

4.1 X-ray diffraction (XRD) characterization

X-ray diffraction (XRD) were utilized analyse the crystalline nature of produced g-C_3N_4, Fe_3O_4 NPs and g-C_3N_4/Fe_3O_4. Figure 4.1a shows the XRD pattern of Fe_3O_4 NPs brag reflection peaks were found at 30.1°, 35.5°, 43.21°, 57.01°, and 62.61°, respectively assigned to (220), (311), (400), (511) and (440) planes, that match precisely with JCPDS No. 19-0629, suggesting that Fe_3O_4 particles have a cubic spinal structure. (Selen et al., 2023). The two separate diffraction peaks of g-C_3N_4 at 2θ around 13.0° and 27.4°, that belong to the (100) and (002) crystal planes, respectively, can be observed in Figure 4.1b. This alignment is exactly in line with the g-C_3N_4 standard XRD pattern (JCPDS 87-1526). The absence of extra peak and sharp peaks in every pattern show that there are no impurities and that the resulting powders are highly crystalline respectively.

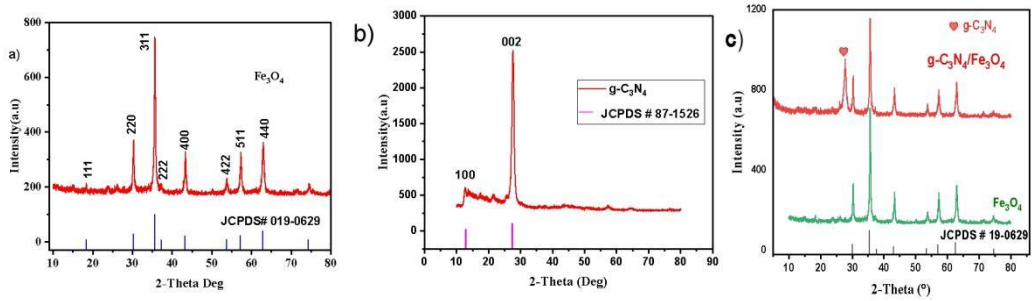

Figure 4.1 XRD patterns of a) bare Fe_3O_4, g-C_3N_4 /Fe_3O_4 NCs b) g-C_3N_4

The successful integration of both nanocalysts without the formation of any secondary phases is confirmed by the g-C_3N_4/Fe_3O_4 NSs' XRD analysis. The distinctive diffraction peaks of Fe_3O_4 that related to the (220), (311), (400), (422), (511), and (440) planes of the spinel cubic structure are clearly visible in g-C_3N_4/Fe_3O_4 ratios, indicating that the crystalline integrity of magnetite is maintained. Additionally, the composites exhibit a semi-broad peak at 27.4°, which is corresponds to the (002) plane of CN, arising from interlayer stacking of its conjugated aromatic structures. The decrement of in XRD peak intensities of both g-C_3N_4 and Fe_3O_4 in the composites suggests a strong interfacial interaction which indicates successful

integration of the two phases, likely enhancing their synergistic properties for photocatalytic or electronic applications (Feyie et al., 2024).

The mean crystallite size has been calculated by using the Debye-Scherrer equation (eqn 4.1). The calculations showed average crystallite sizes of 19.6, 10.5, and 15.26 nm for Fe_3O_4 , g-C_3N_4, and C_3N_4/Fe_3O_4, respectively, demonstrating a slight reduction in the size of the C_3N_4/Fe_3O_4 composite relative to that of pristine g-C_3N_4 .

$$Z = \frac{0.94\lambda}{\beta Cos\theta} \qquad 4.1$$

Where, Z is the mean crystallite size, λ is wavelength, θ is the Bragg diffraction angle, and β is the peak width at half-width maximum.

Table 4.1. The average crystalline size of synthesized nanomaterials

Materials	**Peak position**	**FWHM**	**Crystallite size (nm)**	**Averege crystalize size (nm)**
Fe_3O_4	30.26119	0.4101	20.9586	
	35.64951	0.4274	20.3949	19.40
	62.94677	0.5793	16.7940	
g-C_3N_4	27.60267	0.8504	10.05	10.05
g-C_3N_4/Fe_3O_4	27.72088	0.44123	19.3691	
	35.63212	1.06104	8.2144	
	62.91368	0.53485	18.1862	15.26

4.2 Morphological characterization

4.2.1 Scanning electron microscopy (SEM) Analysis

The surface morphology of synthesized Fe_3O_4, g-C_3N_4 and g-C_3N_4/Fe_3O_4 NSs were investigated using FE-SEM, as depicted in Figure 4.2. The pure C_3N_4/Fe_3O_4 nanostructure shows the developments of nanoparticles with no agglomeration, as shown as (Figure 4.2c,d). The pristine g-C_3N_4 exhibit the lamelar nanosheet structure (Figure 4.2a) and The spherical Fe_3O_4 nanoparticles were grown on g-C_3N_4 nanosheet.

In comparison to the bare Fe_3O_4, the g-C_3N_4/Fe_3O_4 composite shows a more uniform dispersion of particles with less agglomeration, suggesting that the g-C_3N_4 matrix has improved particle stabilization. This porous and interconnected structure is advantageous for applications like photocatalysis, adsorption and sensor as it promotes improved accessibility of active sites, boosted light interaction, and efficient charge transfer.

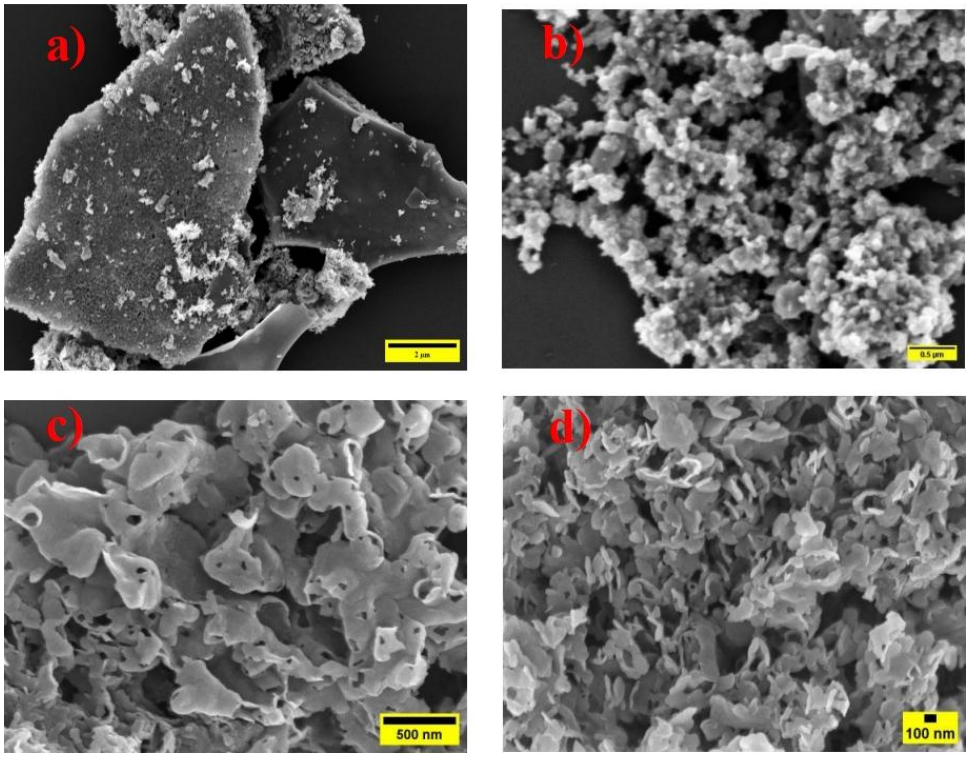

Figure 4.2 SEM analysis of a) g-C_3N_4 b) Fe_3O_4 c,d) g-C_3N_4/Fe_3O_4

4.2.2 FESEM-EDX Analysis

EDX spectrum and elemental mapping analysis were used evaluating the elemental composition and distribution of synthesized nanocomposite. According to the study's results the elements Fe, and O can be identified as shown in (figure 4.3). The element C, and N can be identified in addition to Fe and O as shown in (figure 4.4) Fe_3O_4 nanoparticles were successfully loaded onto the g-C_3N_4 surface, as shown by the mapping analysis in (Figure 4.4). The weight % of Fe, N, C, and O in g-C_3N_4/Fe_3O_4 sample were determined to be 21.16, 24.78, 38.96 and 15.10%, respectively. This analysis also showed that the magnetic Fe_3O_4 nanoparticles were

uniformly distributed on the C_3N_4 surface (Figure 4.4), which will be favorable for photocatalytic and adsorption application.

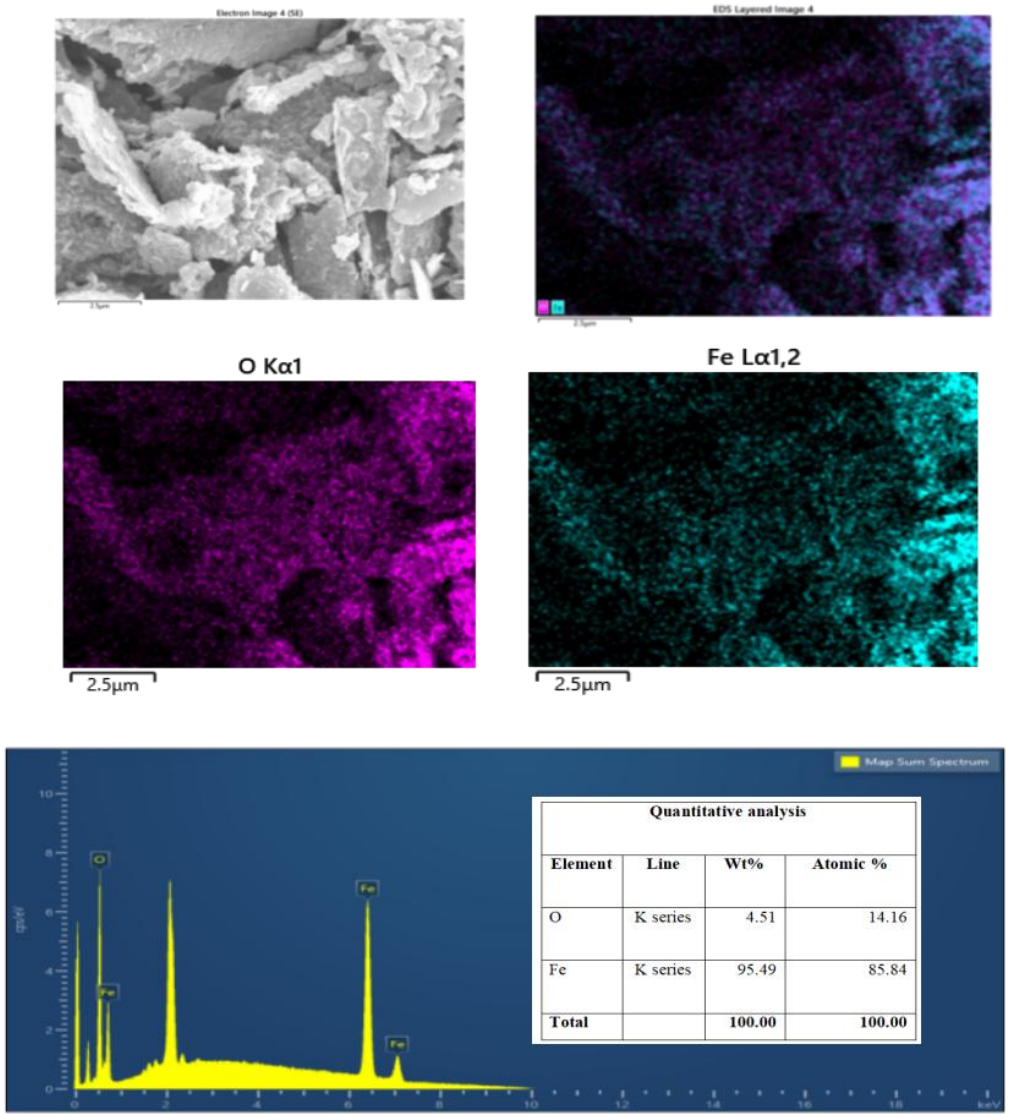

Figure 4.3 FESEM-EDX of bare Fe_3O_4

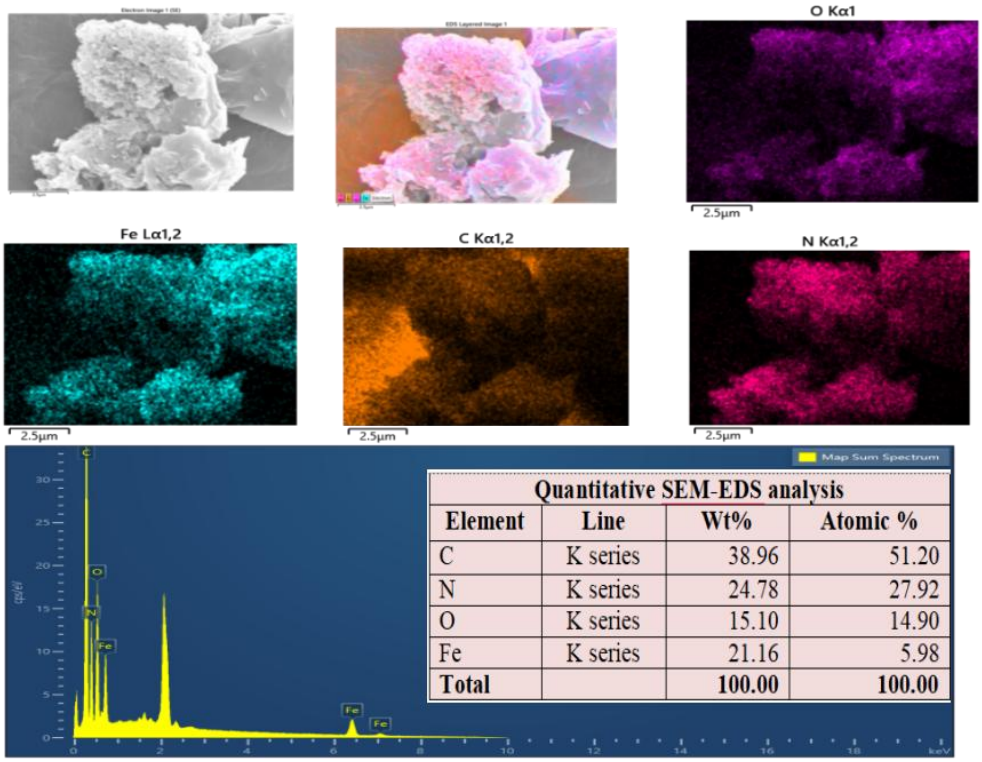

Quantitative SEM-EDS analysis			
Element	**Line**	**Wt%**	**Atomic %**
C	K series	38.96	51.20
N	K series	24.78	27.92
O	K series	15.10	14.90
Fe	K series	21.16	5.98
Total		**100.00**	**100.00**

Figure 4.4 FESEM-EDX image of CN/Fe_3O_4

4.2.3 X-ray photoelectron (XPS) analysis

X-ray photoelectron (XPS) measurements were utilized to analyze the elemental composition and oxidation states of synthesized materials. The C_3N_4/Fe_3O_4 XPS survey spectrum, displayed in Figure 4.5, indicate the presence of the Fe, C, O, and N elements, which is consistent with SEM-EDAX result. A high-resolution Fe 2p core-level spectrum showing the Fe $2p_{3/2}$ and Fe $2p_{1/2}$ core levels is shown in Figure 4b. According to (Ai et al., 2019), the two Fe 2p peaks are doublets that may be deconvoluted into two distinct peaks, indicating the presence of both Fe^{3+} and Fe^{2+} species in magnetic Fe_3O_4. Fe^{3+} is represented by the peaks centered at 710.0 and 723.50 eV, whereas the presence of Fe^{2+} is indicated by the peaks centered at 711.9 and 725.5 eV of the corresponding core levels. Furthermore, the presence of both Fe^{3+} and Fe^{2+} states in magnetite is indicated by the satellite peak centered at 717.5, and 731 eV which indicate mixed Fe^{2+}/Fe^{3+} valence state and further confirm the synthesized material is magnetite. The deconvulated O1s peak separated in to three distinct peak centered at 529.4, 530.9 and 533 eV which were attributed to oxygen

anion (O_2^-) in Fe_3O_4, hydroxide (OH^-) in the surface of metal oxide and specifically adsorbed H_2O, respectively, Which is math with other findings (Ai et al., 2019).

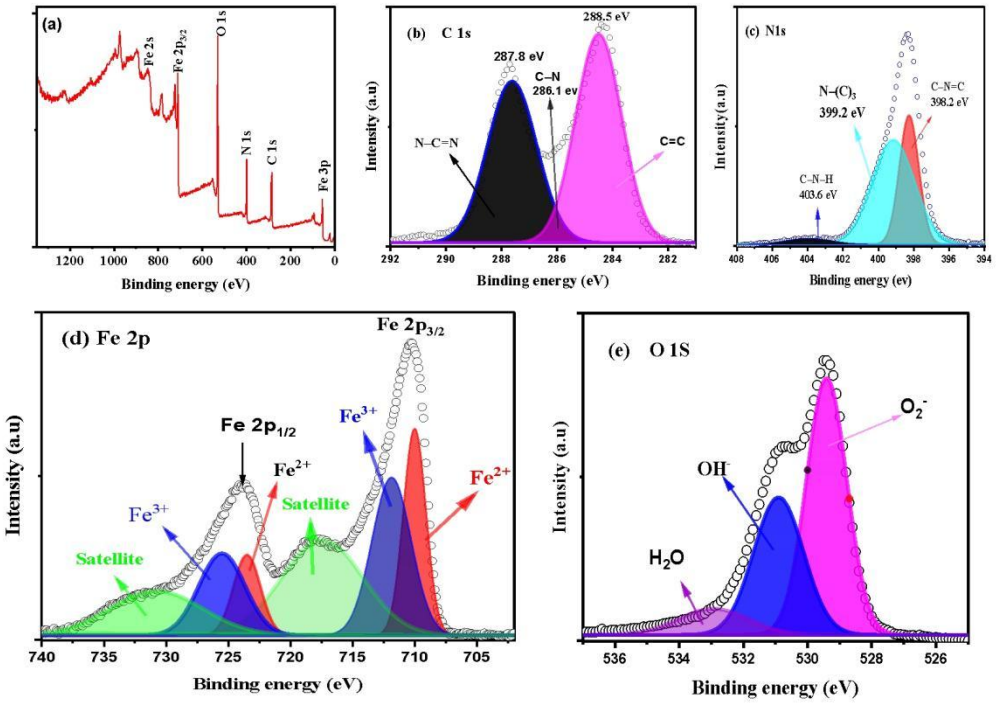

Figure 4.5 XPS characterization : (a) full spectra (b) C1s c) N1s, (d) Fe2p, (e) O1s, of C_3N_4/Fe_3O_4 magnetic nanostructure

In C_3N_4 the two significant peaks centered at 288.5 and 287.8 eV can be identified in the C 1s spectra as shown in the Figure 4.5b, it deconvoluted, into three peaks that represent carbon in three distinct conditions with the third peak centered at 286.1 eVs. The Sp^2-bonded carbon (N–C=N) is responsible for the main peak, which is located at 287.8 eV. The other peaks, which are typically seen on the XPS spectra of g-C_3N_4, are located at 286.1 and 288.5 eV and indicate C in C–NH_2 and C=C bonds, respectively. These results align with the three carbon types in g-C_3N_4 that identified by FTIR analysis result and (Feyie et al., 2024). The deconvoluted high-resolution N 1s spectra depicted in Figure 4.5c show the three separate peaks centered at 398.3, 399.2, and 403.0 eV. The sp^2 hybridized aromatic nitrogen bound to carbon (C–N=C) is shown by the peak with a center at 398.4 eV. The nitrogen in N–(C)3 is identified by the peak centered at 399.1 eV, whereas the N in C–N–H is identified by a small signal with a binding energy of 401.0 eV (Feyie et al., 2024) as shown in figure 4.5c.

4.3 Fourier Transform Infrared spectroscopy (FTIR) study

The functional groups and molecular interactions of synthesized pristine C_3N_4, Fe_3O_4 and C_3N_4/Fe_3O_4 magnetic nanostructures were analyzed using Fourier Transform Infrared spectroscopy (FTIR) techniques. In the FTIR spectra depicted in Figure 4.6 pristine Fe_3O_4 shows characteristic peak at 564 cm^{-1} which belongs to the Fe-O stretching vibration in the octahedral sites of the magnetite structure. Furthermore, peaks around 3200 cm^{-1} and 100 cm^{-1} show O-H stretching vibrations, that are mainly described to hydroxyl groups from adsorbed water. Again the pristine g-C_3N_4 shows peak around 3100 cm^{-1} is because of the N–H asymmetric tension vibrations. An observed peak at1630 cm^{-1} is also from C=N stretching which is a characteristics of the conjugate system in C_3N_4 .The several absorption peaks in the 1230–1530 cm^{-1} region correspond to typical stretching modes of C–N and C═N stretching vibrations of the CN aromatic repeating units. The main sharp absorption peaks observed at 810 cm^{-1} is a Breathing mode of s-triazine rings strong evidence of g-C_3N_4 backbone which is align streetwise with literature (Sarp & Yilmaz, 2022).

Decrease in the intensity of peaks in the C_3N_4/Fe_3O_4 composite compared to bare C_3N_4 and Fe_3O_4 and the shift of main Fe-O stretching vibration peaks can be suggest strong molecular interaction between Fe_3O_4 nanoparticles and the C_3N_4.

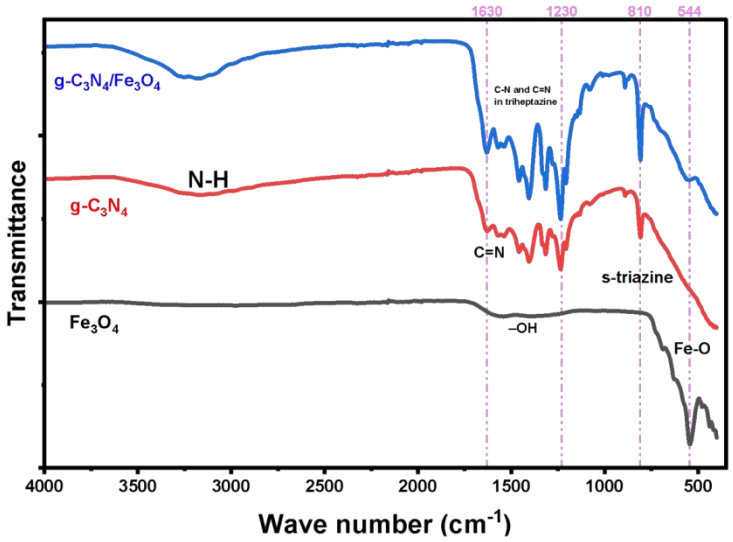

Figure 4. 6 FTIR analysis of synthesized g-C_3N_4, Fe_3O_4 and g-C_3N_4/ Fe_3O_4

4.4 Brunauer Emmett Teller (BET) Surface Area Estimation

The surface area of the produced C_3N_4, Fe_3O_4 and C_3N_4/Fe_3O_4 magnetic nanostructures was determined using the Brunauer emmett teller (BET) techniques, which was performed out with N_2 adsorption-desorption tests. The surface area and pore asize of fabricated magnetic nanocatalysts were estimated using nitrogen sorption measurements and pore-size distribution curves obtained at 77 K with 10 s equilibration Interval.

The calculated BET surface areas for the magnetite, C_3N_4 and C_3N_4/Fe_3O_4 composites were calculated to be 11.2187, 21.1726 and 129.4180 m^2/g, respectively as shown in the table 4.2. The C_3N_4/Fe_3O_4 nanostructure shows a higher surface area (129.4180 m^2/g) than pristine is due to exfoliation of C_3N_4 layers and Fe_3O_4 nanoparticles prevent sheet restacking and create mesopores. This rise the number of exposed active reaction sites, enhancing its catalytic as well as adsorption performance.

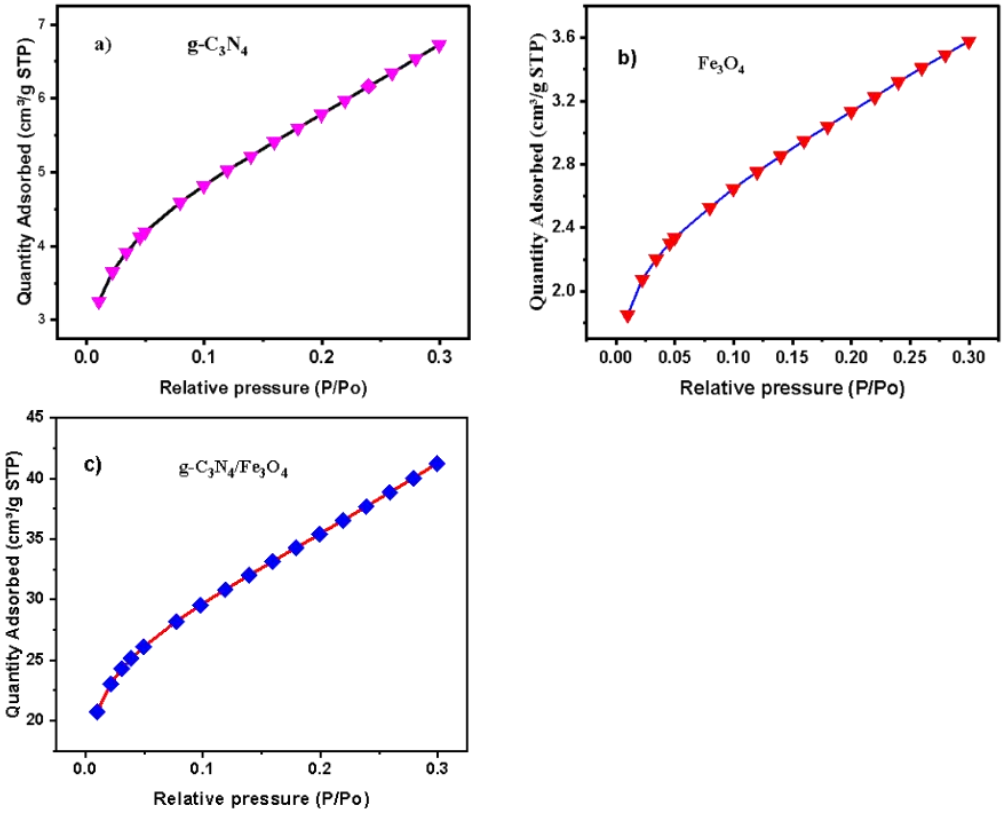

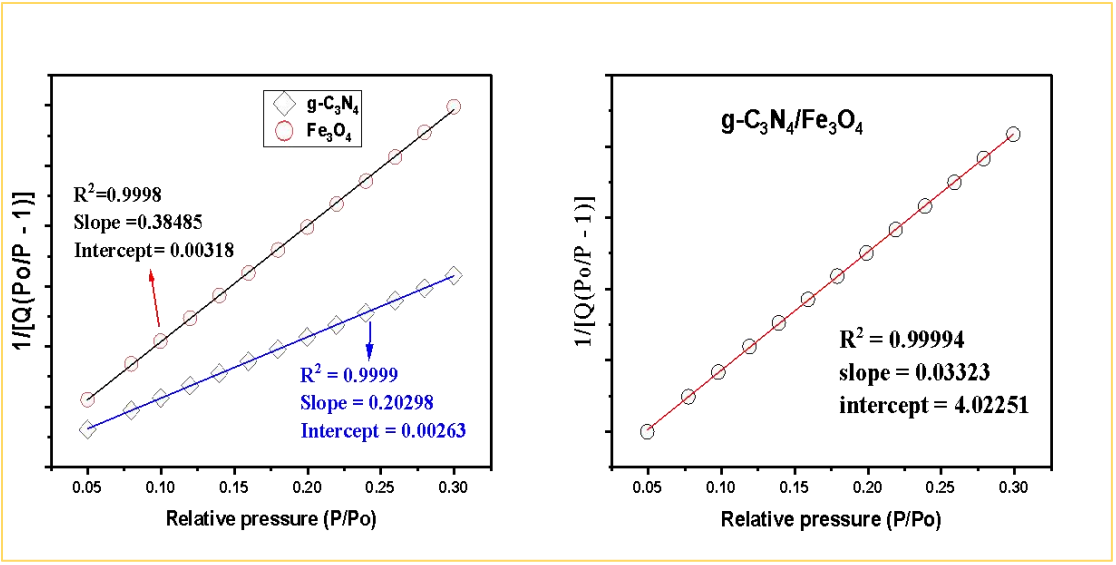

Figure 4.7 N_2 adsorption–desorption isotherms of (a) C_3N_4 b) Fe_3O_4 and c) C_3N_4/Fe_3O_4 d) BET Surface Area Plot

As shown in the table 4.2 below, the Fe_3O_4 has very low surface area (11.2 m^2/g) with high BET Constant value, indicating strong adsorption but few active sites. g-C_3N_4 shows slightly higher surface area (21.2 m^2/g) but is limited by sheet stacking. The g-C_3N_4/Fe_3O_4 composite exhibits a much larger surface area (129.4 m^2/g) and higher monolayer capacity due to exfoliation and mesopore formation. This confirms that Fe_3O_4 nanoparticles prevent restacking of g-C_3N_4 and create more accessible active sites, enhancing catalytic potential and adsorption performance.

Table 4.2 BET Surface Area and porosity Parameters of catalyst.

Catalyst	**Surface area (m^2/g)**	**Mono layer Capacity (Q) (cm^3/g STP)**	**BET Constant (C)**
Fe_3O_4	11.2187	2.5771	121.856809
g-C_3N_4	21.1726	4.8637	78.3019
g-C_3N_4/Fe_3O_4	129.4180	29.7294	83.591902

4.4 Optical characterization

The optical absorption properties of the prepared C_3N_4, Fe_3O_4 and C_3N_4/ Fe_3O_4 catalysts were also studied through UV–vis diffusive reflectance spectroscopy (UV-DRS) and UV–visible spectroscopy study.

Using the Kubelka–Munk equation (equation (1), the optical band gap energy of C_3N_4, Fe_3O_4 and C_3N_4/Fe_3O_4 was determined using UV-DRS in a wavelength range of 200–800 nm and depicted in (figures 4.6 a–e):

$$(F(R)*hv)^{1/2} = A(hv-Eg) \qquad 4.2$$

Where; v is the photon's frequency, h is the Planck's constant, n=1/2 in the power index denotes the indirect transition for a direct band gap, and A is the proportionality constant.

The C_3N_4/ Fe_3O_4 nanostructure showed a lower optical band gap from 1.95 eV, compared to bare C_3N_4 = 2.72 eV as shown in figures. This lower in band gap could be due to the partial incorporation and interaction magnetic Fe_3O_4 onto 2D-C_3N_4. This enhancement promotes stronger visible-light absorption and facilitates charge carrier separation through interfacial electronic interaction between Fe_3O_4 and g-C_3N_4.

From UV-Vis study also the C_3N_4, the C_3N_4/ Fe_3O_4 nanostructures' absorption spectra showed a redshift (band gap narrowing) and higher higher intensity as depicted in the (figure 4.6 f) Which was due to the existance of loaded magnetic Fe_3O_4 material on 2D g-C_3N_4 surface, which also caused this shift and rise in peak intensity. Therefore, g-C_3N_4/ Fe_3O_4 MNCs obtain light in the visible spectral region and could have shown high photocatalytic performance.

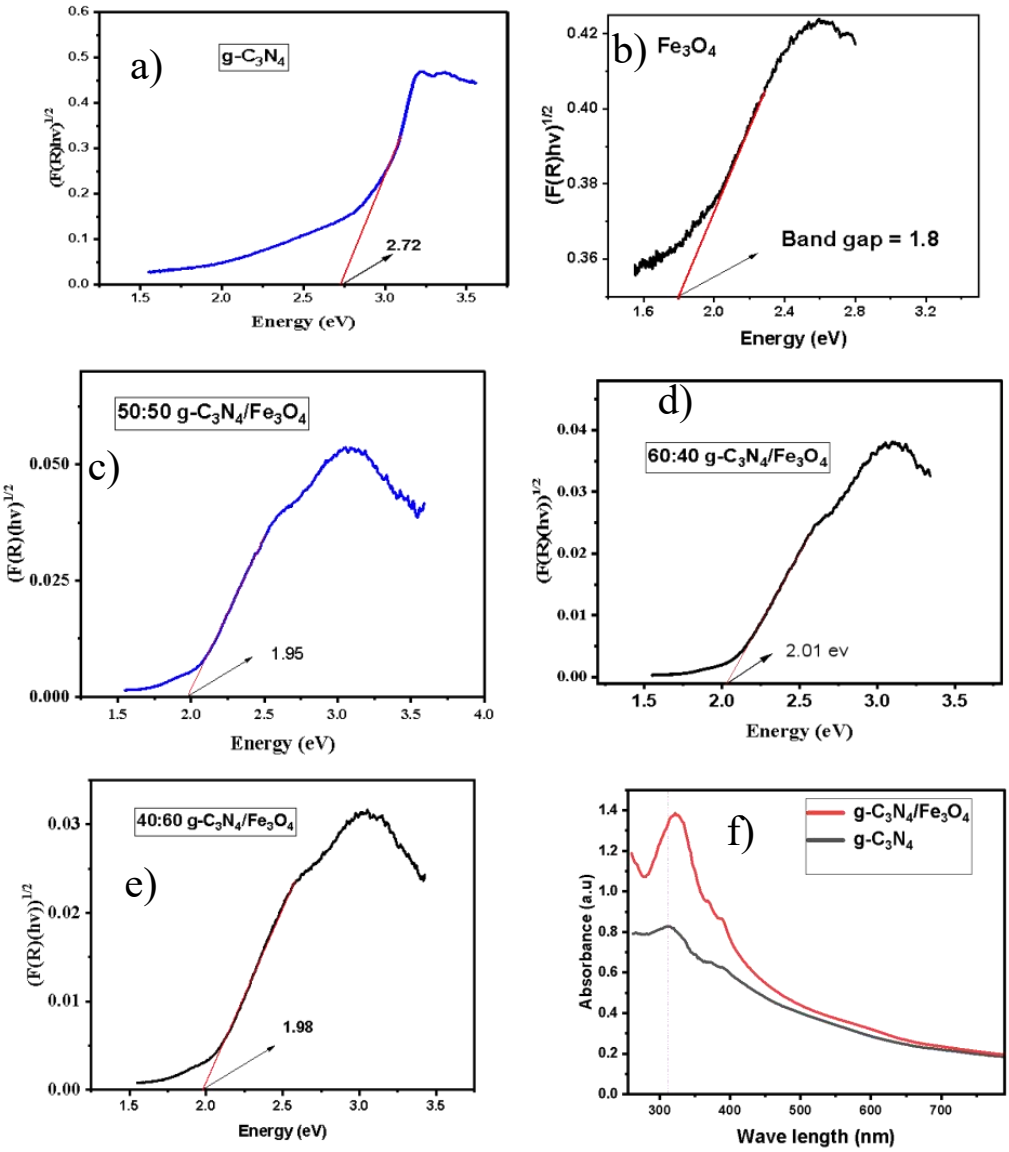

Figure 4. 8 Optical characterization, UV-DRS (a-e) and UV-Vis (f)

4.4.1 Photoluminescence Analysis

The performance of the semiconductor photocatalyst's carrier charge separation activity was examined using photoluminescence (PL) study. As it relates to carrier recombination, the intensity of the PL emission peak is often related with the degree of carrier separation efficiency among the catalysts (Feyie et al., 2024). displays the PL spectra of the g-C_3N_4, and g-C_3N_4/Fe_3O_4 composites with different mass ratio (40;60, 50:50, 60:40 and 70:30) that were measured at a 350 nm excitation wavelength. . The PL spectrum of g-C_3N_4 exhibits a high photoluminescence

intensity, showing a high recombination rate of electron-hole pair. The significant decrease in the C_3N_4/Fe_3O_4 nanostructures PL emission intensity when contrasted to the bare C_3N_4 indicates an improvement in charge separation performance due to the suppression of charge recombination, that may be advantageous for increased photocatalytic work.

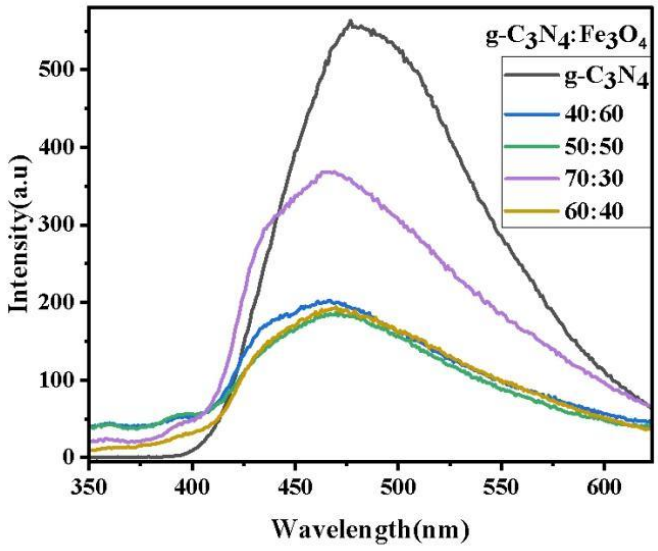

Figure 4. 9 PL spectrum of C_3N_4, C_3N_4/Fe_3O_4 with different ratio

4.5 Electrochemical Characterization

The process of charge transfer and separation at the interface between the electrolyte solution and the drop cast C_3N_4, and C_3N_4/Fe_3O_4 based electrodes were evaluated using electrochemical impedance spectroscopy (Sousa et al.) measurements. Using Ag/AgCl as the reference electrode, and Platinum wire as counter electrode. The EIS measurements were performed out in 0.1 M KOH throughout a frequency range of 100 kHz to 0.1 Hz. The Mott-Schottky experiment was also performed in 0.5 M Na_2SO_3 solution in a potential window of −1.3 to +1V.

The Randle circuit is chosen due to its best represents the electrochemical process occurring at the $Fe_3O_4/g\text{-}C_3N_4$ electrode interface. It consists of solution resistance (Rs), charge transfer resistance (Rct), double-layer capacitance (Cdl), and Warburg impedance (Zw). Rs accounts for the resistance of the electrolyte, Rct represents the electron transfer resistance at the interface, Cdl indicates the capacitive behavior of

the electrode surface, and Zw reflects ion diffusion. The good fitting of experimental EIS data with this circuit confirms that the system follows a typical charge-transfer-controlled process. The decrease in Rct after Fe_3O_4 incorporation suggests improved electrical conductivity and faster electron transfer, enhancing photocatalytic and electrochemical activity. The charge transfer impedance at the electrode–electrolyte interface is represented by the radius of the semicircle of the Nyquist diagram; the smaller the radius of the circle, the better the efficiency of separation of light-generated charge carriers recombination and the faster the interfacial charge transfer rate (Liang et al., 2025). As showns in the (figure 4.10c), Among any of these composite photocatalysts, the nanosphere like g-C_3N_4 /Fe_3O_4 with 1:1 ratio has the lowest impedance and has the best electrical conductivity was. The EIS study show that the g-C_3N_4/Fe_3O_4 had the capacity to separate and transfer photogenerated carriers with excellent efficiency. It exhibits the remarkable photogenic electron-hole pair separation ability of the composite.

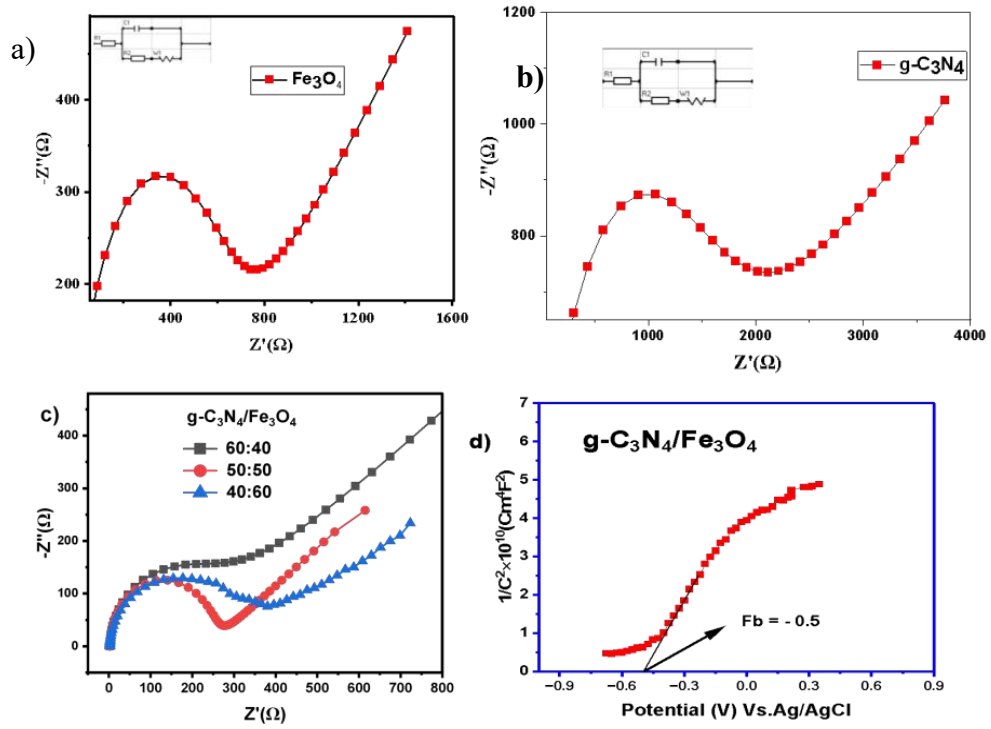

Figure 4.10 Electrochemical characterization, EIS of from (0.1 Hz to 100 kHz) a) g-C_3N_4 b) Fe_3O_4 c) g-C_3N_4/Fe_3O_4 and MS of d) g-C_3N_4/Fe_3O_4

The Mott-Schottky (Bai et al.) analysis was also used to determine the electrical band potentials and structures of the produced samples as shown in the (figure 4.10d) . The Resulting plots for g-C_3N_4, g-C_3N_4/Fe_3O_4 indicate that a positive slope, which indicates its n-type semiconducting feature. The flat band potentials (E_{fb}) with respect to Ag/AgCl and RHE substrate were also calculated by extending the linear section of the line toward the x-axis from the MS plot. Previous research (Endeshaw et al., 2025) has shown that the flat-band potential (Efb) of p-type and n-type semiconductors may use to calculate their valence band potential (EVB) and conduction band potential (ECB), respectively.

4.6 Adsorption of PSMP onto g-C_3N_4/Fe_3O_4 Magneticnanosphere

4.6.1 Effect of pH on adsorption

The adsorption of PS microplastics on 2D g-C_3N_4/Fe_3O_4 MNS is affected by pH due to surface charge interactions. The pH of the PS solution was adjusted to 4, 5, 6, 7, and 8 with 0.1 M HCl and 0.1M NaOH to analyse the adsorption effect of PSMP on 2D g-C_3N_4/Fe_3O_4. Other experimental parameter were set according to the conditions explained in the 'Adsorption studies' section. Increase in the pH value, the removal efficiency of MP and the adsorption capacity of the 2D g-C_3N_4/Fe_3O_4 raised initially when pH raised from 4 to 6 and then declined when pH raised from 6 to 8. At lower pH, the surface of g-C_3N_4/Fe_3O_4 becomes positively charged due to protonation of amide group in g-C_3N_4 as shown on point of zero charge plot (figure 4.11b), while PS microplastics generally possess a negative surface charge, leading to some electrostatic attraction. However, the high concentration of H^+ ions at acidic pH also competes for active adsorption sites, reducing overall efficiency. In alkaline conditions (pH 7–8), the surface becomes increasingly negatively charged, which causes electrostatic repulsion with the negatively charged PS microplastics, thus decreasing adsorption performance. At pH = 6, the 2D g-C_3N_4 /Fe_3O_4 exhibit optimum removal efficiency 80% at the condition of 0.1g catalyst dose, 30 mg/L PS initial concentration and one hour contact time.

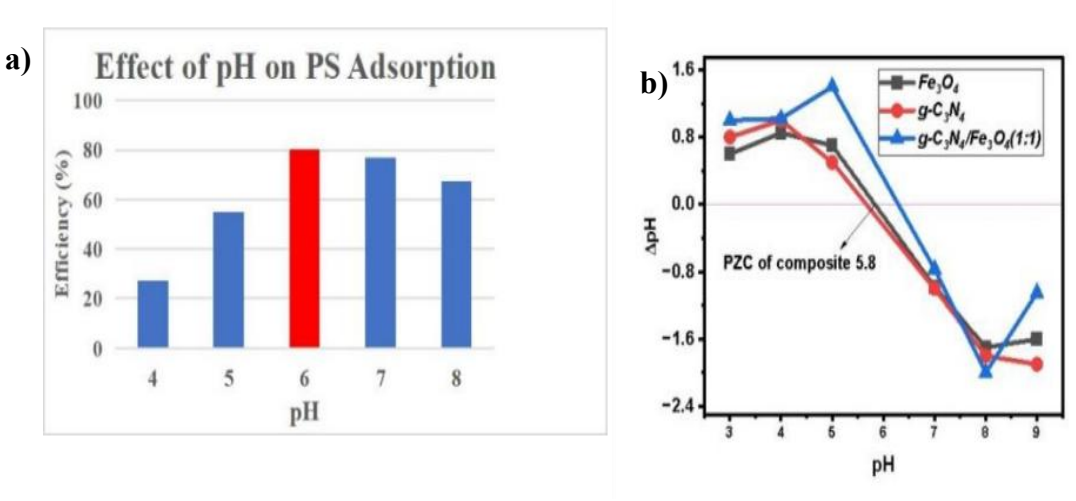

Figure 4.11 Plot of a) effect of pH on adsorption (0.1g, catalyst, 30 mg/L, for 1hr) b) point of zero charge analysis

4.6.2 Effect of adsorbent dosage

The g-C_3N_4, Fe_3O_4, and g-C_3N_4/Fe_3O_4 magneto nanocomposite's adsorption capacity and adsorption efficiency was investigated by changing the adsorbent amount between 0.05g and 0.2 g, at pH 6, 30 mg/L PS initial concentration and contact time up to 225 min as shown in (Figure 4.12). The efficacy of PSMP removal was greatly raised by increasing the dosages of all nanoadsorbent up to 0.15 g/L. But after then, the removal efficiency was decreased. This could be related to the availability of greater number of active adsorption sites. Consequently, these sites may remain saturated after this optimum adsorbent dosage. There is also agglomeration of adsorbent particles that may also cause for blocking of PS diffusion paths.

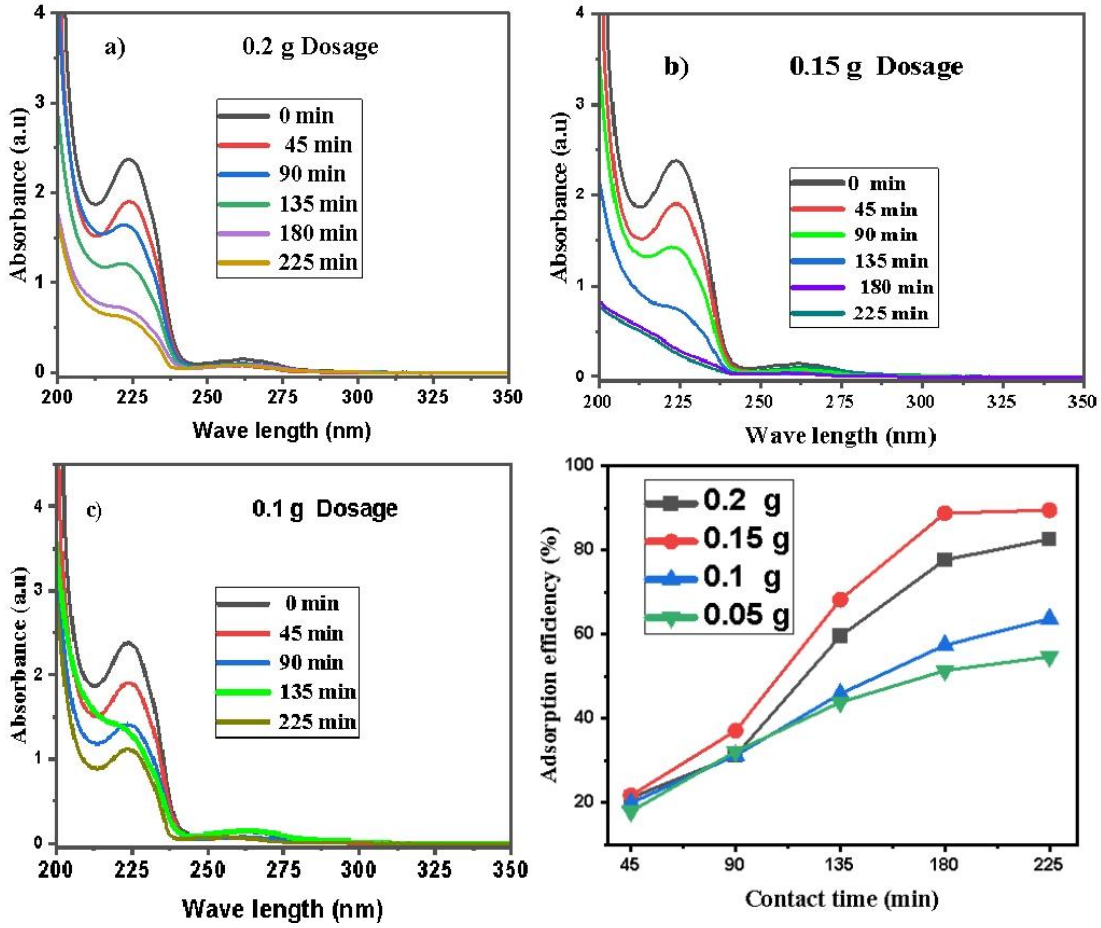

Figure 4.12 Effect of adsorbent dosage a) 0.2g, b) 0.15g c) 0.1g d) 0.05g e) adsorption efficiency

4.6.3 Effect of PS initial concentration

The adsorption efficiency of g-C_3N_4/Fe_3O_4 increases from 56 to 68 when the initial concentration of PS microplastics is changed between 20 and 40 mg/L, at pH=6, adsorbent dosage 0.15 g and contact time of 135 min as depicted in the (Figure 4.13). This is due to fewer molecules interact with the catalyst at lower PS concentration, leaving many active sites unused and leading to a low reaction rate, and hence increase with increasing PS initial concentration to 40 mg/L. After this optimum initial concentration increasing the concentration of PS, cause the saturation of this active sites, leading in a decrease in the removal performance of the adsorbent.

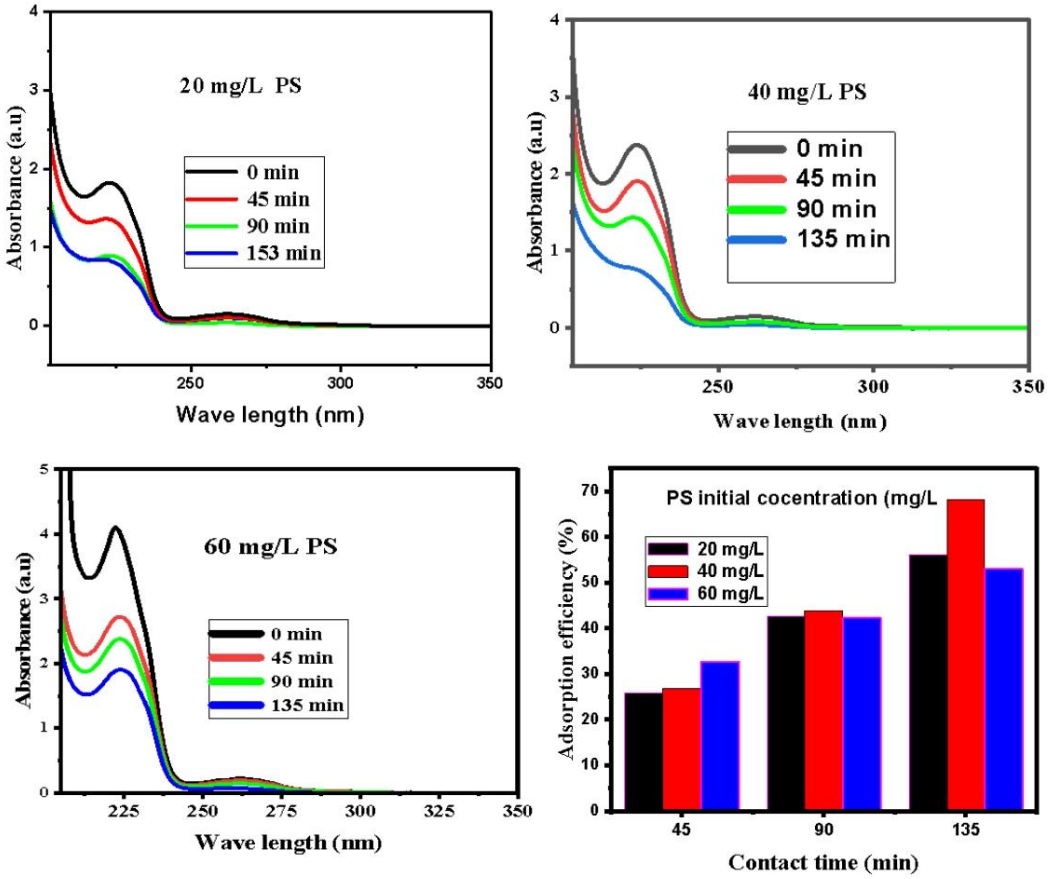

Figure 4.13 Effect of initial PS concentration on adsorption performance

4.6.4 Adsorbent comparison and influence of the Magnetic Field in the Adsorption Process

As shown in the figure 4.14a the adsorption performance of synthesized Fe_3O_4, C_3N_4 and C_3N_4/Fe_3O_4 were tested at optimum condition(pH 6, adsorbent dose, 0.15g/L, AMX concentration 40mg/L) at different contact time (from 0 to 225 min). The C_3N_4/Fe_3O_4 nanosheet exhibit higher degradation efficiency (87%) compared to bare magnetite and graphitic carbon nitride. This is due to band gap decrement of C_3N_4 from 2.72 to 1.95, and presence of high surface area (129 m^2/g) of 2D nanocomposites discussed in BET analysis portion. The result also significantly show the fast electron hole recombination limitation of g-C_3N_4 and very low band gap that is inconvenient to light harvesting of magnetite, which is solved by formation n-n heterojunction between magnetite and 2-D graphitic carbon nitride semiconductors.

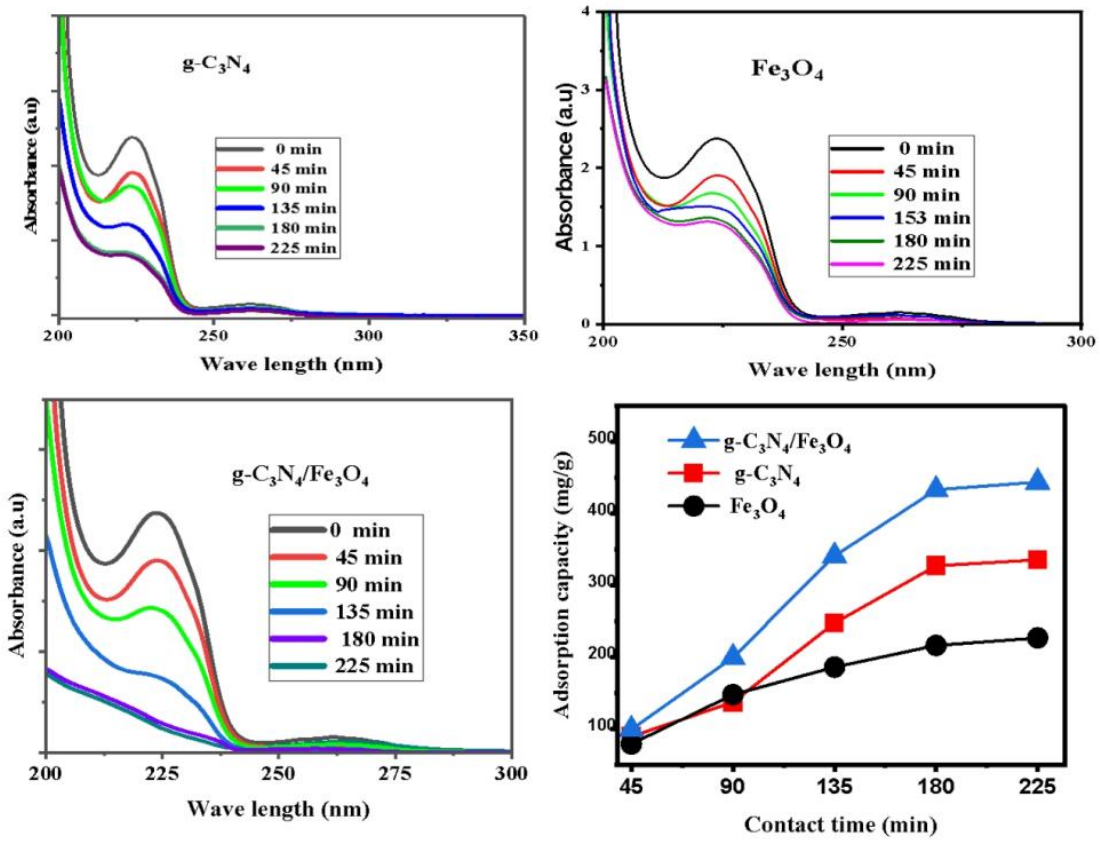

Figure 4.14a Adsorbent comparision at optimum conditions

The removal percentage increased from 87% to 92.88% when a magnetic field was applied, indicating that the introduction of the magnetic field may improve the interaction between polystyrene and g-C_3N_4/Fe_3O_4, either by improving the adsorbent's dispersion or changing its surface characteristics. The possibility of magnetic fields to modify the adsorption strength of intermediates and the spin configuration of active sites allows for spin-selective electron transfer during reactions, which in turn improves reaction kinetics, which more explained according to (Sousa et al., 2025) study.

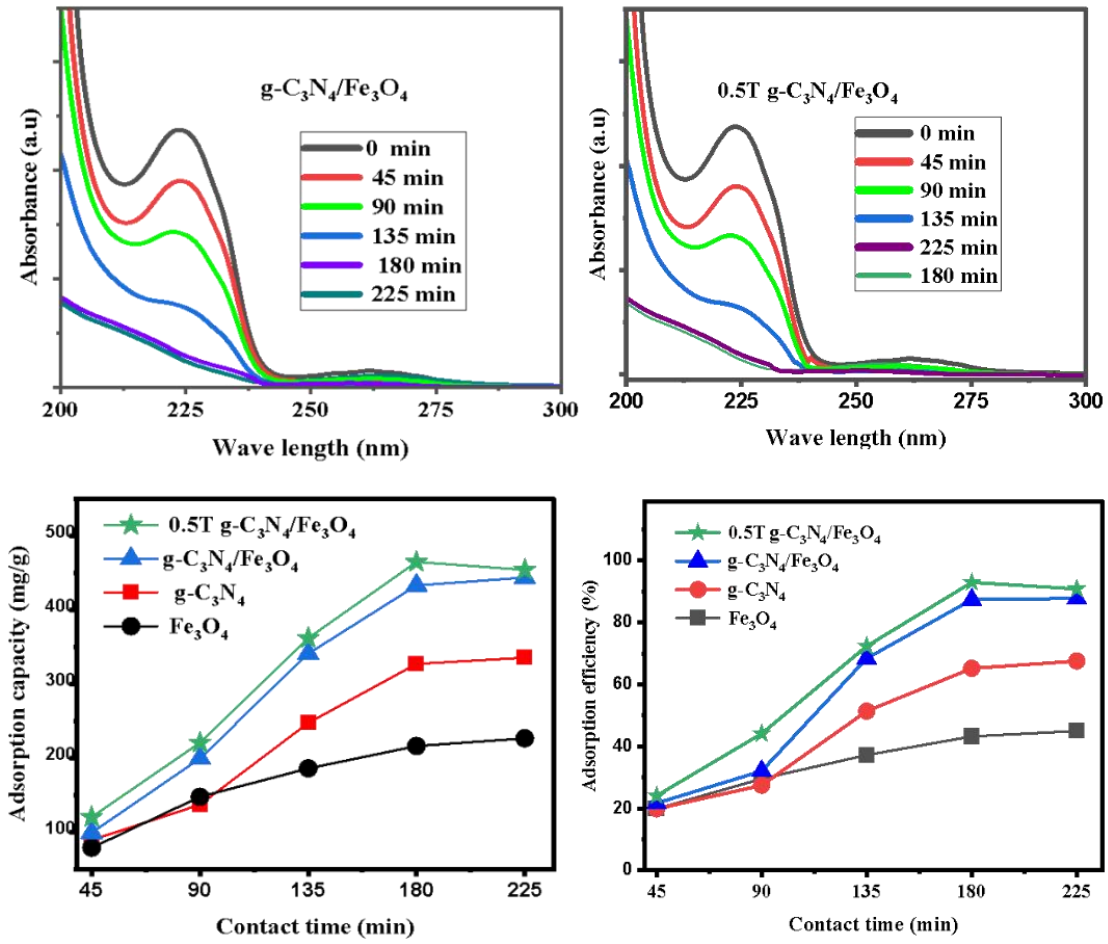

Figure 4.14b Effect of MF on adsorption process

4.7 Kinetic study of the PS adsorption

The kinetic model plot and the estimated kinetic parameters of PFO are illustrated in (Figure 4.15) and table 4.3 respectively. Pseudo First-order kinetics (PFO) were fitted to match the laboratory obtained data in order to evaluate the rate of adsorption and adsorption behavior of the C_3N_4, Fe_3O_4, C_3N_4/Fe_3O_4 and 0.5T MF applied C_3N_4/Fe_3O_4 nanostructures.

The equation for PFO kinetics;

$$\ln(q_e - q_t) = \ln q_e - k_1 t \qquad 4.2$$

The kinetic parameter shows that the adsorption of polysyrene microplastic on all adsorbents are well aliened with pseudo first order kinetic model with 0.96, 0.962, 0.973, 0.961 for g-C_3N_4 , Fe_3O_4 , g-C_3N_4/Fe_3O_4 and 0.5 T g-C_3N_4/Fe_3O_4 respectively as shown in the (Figure 4.13). Thus, the PFO kinetic model suggests that the step

which controls the rate of adsorption is controlled by physiosorption processes such as van der Waals forces, electrostatic attraction, and hydrogen bonding. The speed of adsorption corresponds to the number of empty sites. The rate of reaction for the magnetic force enhanced g-C_3N_4/Fe_3O_4 composite adsorption was found to be 1.12, 1.5 and 1.6 times that of C_3N_4/Fe_3O_4 and pristine C_3N_4 and Fe_3O_4 , respectively, showing enhancement performance and rates of adsorption as 0.5T C_3N_4/Fe_3O_4 magneticnanostructure over either the pristine C_3N_4, Fe_3O_4 and even than C_3N_4/Fe_3O_4 composite.

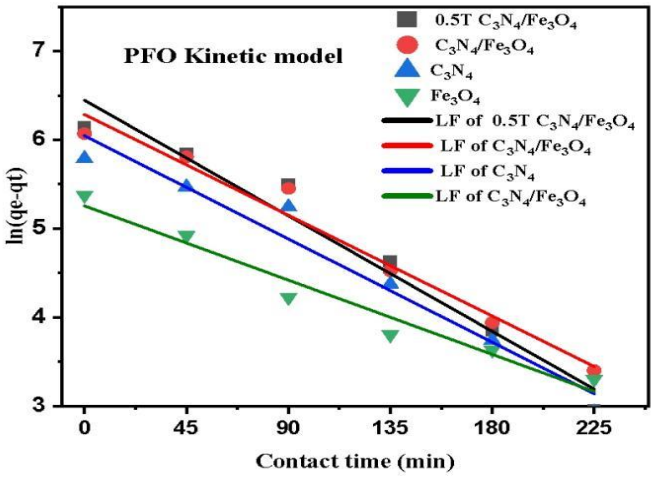

Figure 4.13 Kinetics study of PS adsorption

The calculated adsorption capacity at equilibrium time qe value was 422.7, 191.92, and 537.41 mg/g for C_3N_4, Fe_3O_4 and C_3N_4/Fe_3O_4 respectively, while after exposing the C_3N_4/Fe_3O_4 magnetic nanostructure to 0.5T external MF the qe increased to 630.19 mg/g as shown in the table 4.3 below.

Table 4.3 Adsorption kinetic parameters for adsorption of PS microplastics onto different nanoadsorbent.

Parameter	**C_3N_4**	**Fe_3O_4**	**C_3N_4/Fe_3O_4**	**0.5T C_3N_4/Fe_3O_4**
R^2	0.96	0.962	0.973	0.961
q_e (mg/g)	422.7411	191.918	537.4039	630.19
k_1 (min−1)	0.01262	0.0093	0.01292	0.01446

4.8 Isotherm model study of adsorption

The Freundlich, Temkin, and Langmuir isotherm models were fitted to study the association between the amount of AMX adsorbed and the AMX concentration at equilibrium. Langmuir isotherm model Considering uniform adsorption sites dispersed through the adsorbent surface. In this model, when the adsorbate occupies a site, adsorption cannot proceed beyond the monolayer. An equation of adsorption for this model is expressed as;

$$\frac{Ce}{qe} = \frac{1}{q\,max\,Kl} + \frac{Ce}{qmax} \qquad 4.3$$

where q_{max} ($mg \cdot g^{-1}$) is the maximum adsorption capacity of the adsorbate and K_L ($L \cdot mg^{-1}$) is the affinity constant, which is related to the adsorption binding energy.

Another empirical equation which describes isothermal parameters is the Freundlich model. This equation makes an assumption that adsorption on a heterogeneous surface can be caused by a multilayer adsorption process. The Freundlich equation is expressed as

$$\ln qe = \ln Kf + \left(\frac{1}{n}\right) \ln Ce \qquad 4.4$$

Where K_f is Freundlich model adsorption constants and n is the adsorption-driving force ***(0 ≤ 1 n < 1)***.

The basic concept of the Temkin isotherm model is that the heat of every adsorbate molecule in a layer is linearly reduced by adsorbent–adsorbate interactions. Additionally, there is a homogeneous distribution of the absorbent–adsorbate sites' maximum binding energy. The equation also as;

$$qe = \frac{RT}{b} \ln A + \frac{RT}{b} \ln Ce \qquad 4.5$$

Where, b is the highest binding energy, A is the equilibrium binding constant, T is the temperature, and R is the universal gas constant (8.314 J mol^{-1} K^{-1}).

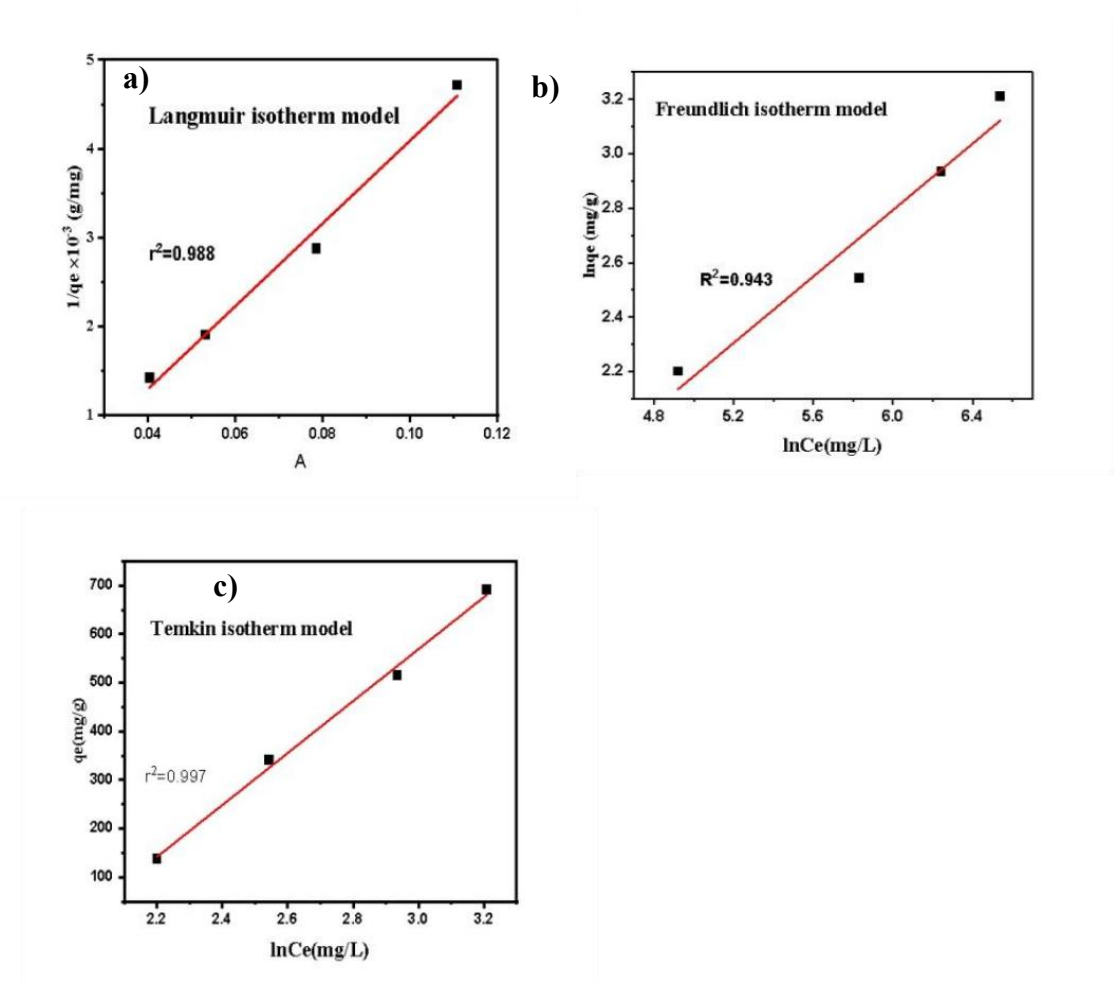

Figure 4. 14 Adsorption isotherm model a) Langmuir b) Freundlich c) Temkin

The synthesised 2D g-C_3N_4/Fe_3O_4, magnetic nanostructures isothermal model study were performed on AMX adsorption by fitting three models, including Langmuir, Freundlich, and Temkin as shown in the (figure 4.16) and Table 4.4 summarizes the calculated variables corresponding to the three models. Based on the data analysis, the Langmuir model fit the data better for AMX adsorption, as indicated by its higher R^2 (0.988) value, which suggested the monolayer sorption capacity and the uniform spread of the active sites on the surface of the g-C_3N_4/Fe_3O_4 magnetic nanoadsorbent. The Freundlich adsorption intensity parameter, 1/n which is 0.62, indicates the favourability of the adsorption process. The experimental data fits the Temkin isotherm very well with R^2 0.997 with Temkin adsorption constant (bT=4.64 J/mol) which indicate the adsorption process is dominated by physisorption, meaning weak interactions such as van der Waals, hydrogen bonding, and π–π stacking.

Based on the calculations, the g-C_3N_4/Fe_3O_4 adsorbent's maximum monolayer adsorption capacity (qmax) is 1201.7 mg/g for 40 mg/L of PS solution.The significant q_{max} suggest that the g-C_3N_4/Fe_3O_4 MNS Serves as an excellent adsorbent to remove PS microplastics in the water environment.

Table 4.4 Isothermal parameters for adsorption of PSMPs onto g-C_3N_4/Fe_3O_4 MN

Isotherm model	Parameters	Values
Langmuir	R^2	0.98863
	qmax (mg/g)	1201.7
	KL (L/mg)	0.018
Freundlich	R^2	0.9
	1/n	0.62
	Kf (L/mg)	7.39
Temkin	R^2	0.997
	b_T (J/mool)	4.64
	AT (L/mg)	0.1446

4.9 Mechanisms of PS adsorption on g-C_3N_4/Fe_3O_4 MNSs

As shown by FTIR analysis, the confirmed presence of particular chemical compositions and surface functional groups on the pine resin extract greatly enhances the mechanism of PSNP adsorption onto g-C_3N_4/Fe_3O_4 MNPs, which is primarily driven by a combination of physicochemical interactions (Figure 4.17a).The π-π interaction has also been involved in the adsorption mechanism by previous research studies (Karunattu Sajan et al., 2024). Therefore, as shown in (Figure 15), the strong interfacial bonding and π-π interaction between PS MPs and the g-C_3N_4/Fe_3O_4 nanocomposite may be responsible for their adsorption. Furthermore,g-C_3N_4's properties which come from the presence of sp^2 hybridized carbon atoms that help it interact with the hydrophobic organic molecules of polystyrene microspheres, which causes aggregates to form van der Waals force (AbuMousa et al., 2022). By building targeted and directed linkages, the possibility of hydrogen bonding which is enabled

by functional groups added to the PSNPs or the nanoparticles further enhances the adsorptive attachment (AbuMousa et al., 2022). Furthermore, depending on the pH of the solution environment, electrostatic attractions are important, particularly when the g-C_3N_4/Fe_3O_4 MNPs are charged and interact with any charged groups on the PSNPs.

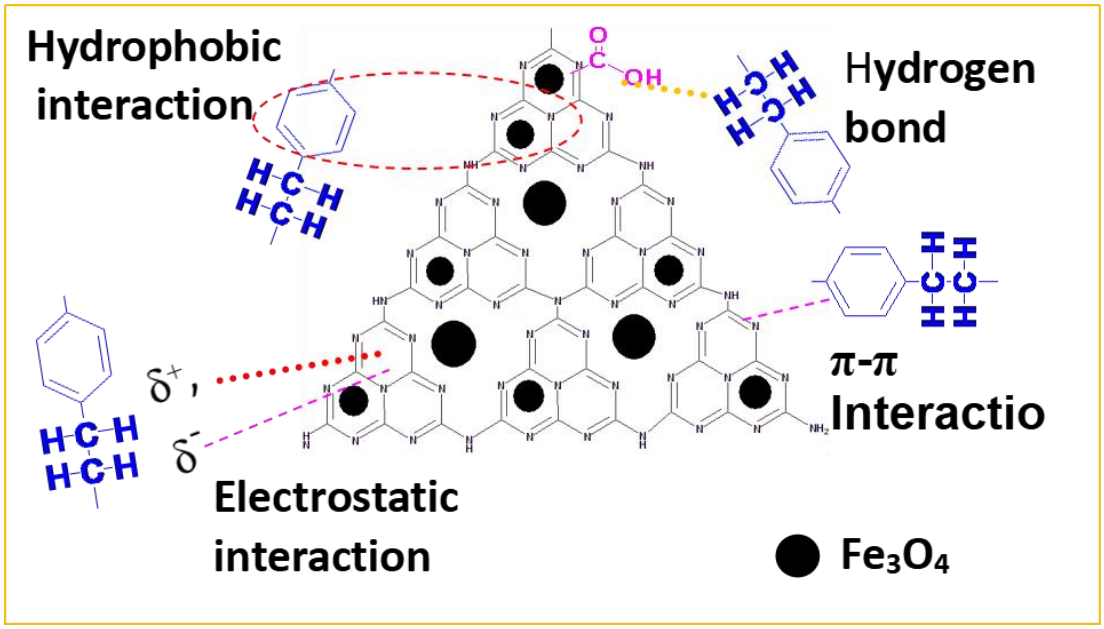

Figure 4.15a Mechanisms of PS adsorption on g-C_3N_4/Fe_3O_4

The external magnetic field mainly enhances the adsorption of PSMP's onto magnetically active C_3N_4/Fe_3O_4 nano-sheet by optimizing the surface interactions and particle transport. The Kelvin force generated under the magnetic gradient produces pressure, which push PS microplastic molecules toward the magnetically active C_3N_4/Fe_3O_4 reactive-sites, increasing surface accumulation. The Lorentz force and hydrodynamic effects improve particle motion and fluid mixing, reducing boundary layer resistance and enhancing contact between adsorbent and microplastics as shown in the (Figure 4.17b). Inaddition, the magnetoresistance effect facilitates better electron mobility and interfacial polarization, strengthening electrostatic and van der Waals interactions between PS and the composite surface. Together, these magnetic phenomena rearrange particles, accelerate diffusion, and promote stronger adsorption affinity, resulting in more efficient and rapid PS removal.

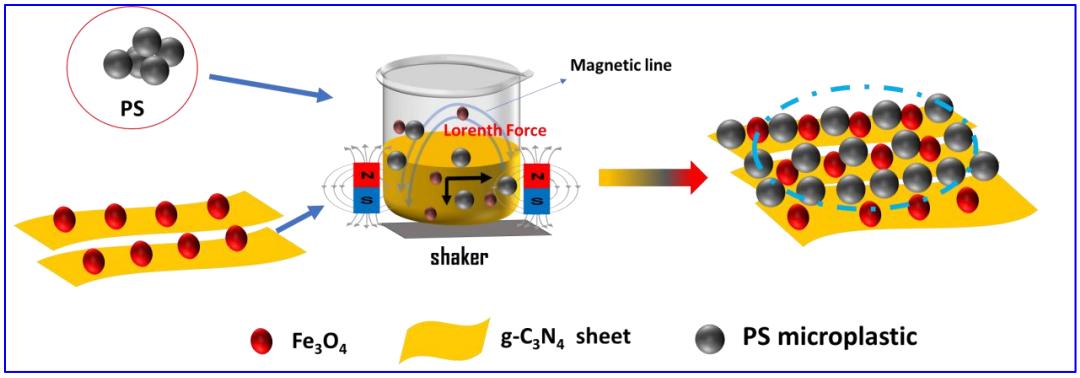

Figure 4.17b Mechanisms of MF enhance adsorption of PS on g-C_3N_4/Fe_3O_4

4.9.1 Adsorbent Re-usability test

Adsorption–desorption cycles were used to evaluate the material's reusability from its practical use. To isolate the adsorbed particles, the g-C_3N_4/Fe_3O_4-PS complex was treated with a 50:50 ethanol water solvent and sonicated for 20 minutes. Then after magnetically separating the adsorbent from the solution, it was then rinsed with a 2:1 ethanol and distilled water mixture, dried at 70 °C, and then dispersed in a fresh PS microplastic solution for another cycle. At a concentration of 40 mg/L PS, four successive adsorption–regeneration cycles were carried out. The removal efficiency maintained to rise above 70% after four cycles, depicted in (Figure 4.18). This study showed that g-C_3N_4/Fe_3O_4 is a remarkable PS adsorbent due to its remarkable reusability. In-Comparison, the 0.5 T external magnetic field applied nanoadsorbent shows higher removal efficiency than the composite, but after repeated cycle use they become equal efficiency, due to the gradual loses magnetic properties and responses due to surface modification and partial aggregation with PS complex, which makes the percentage removal efficiency similar for both cases.

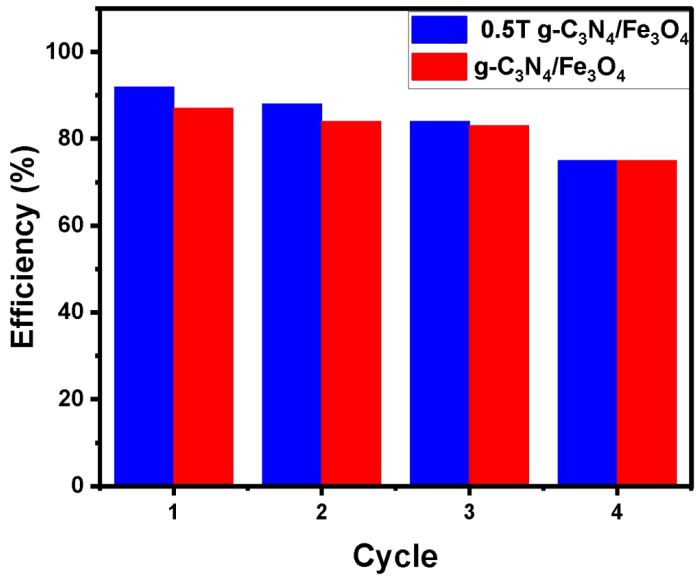

Figure 4.16 Reuablity and stablity of g-C_3N_4/Fe_3O_4 nanoadsorbents

To assess the potential of the fabricated CN/Fe_3O_4 material for microplastic adsorption, a comparison with previous reported adsorbents was performed. Considering five important parameters; microplastic type, adsorption capacity (mg/g), isotherm model, kinetics and efficiency, they exhibit Table 4.5 systematically investigated the new material against the most recent adsorbents.

Table 4.5 the comparative performance of g-C_3N_4/Fe_3O_4 nanoadsorbent with other literature for polystyrene microplatic adsorption.

Catalyst	**qmax (mg/g).**	**isotherm/kinetic**	**Efficiency%**	**Ref.**
Ni/rGO	1250	Langmuir/PSO	82	(Karunattu Sajan et al., 2024)
sawdust-ACs	40.84	Freund/PSO	79	(Sanz-Santos et al., 2025)
PR@ Fe_3O_4 MNPs	454.55	Langmuir/PS		(Matar et al., 2024)
20 mT SA/MXene/CFO	CIP	by 24.19 Under RMF		(Ren et al., 2021)
g-C_3N_4/Fe_3O_4	433.05	Langmuir/PFO	87.4	This work
0.5T C_3N_4/Fe_3O_4	464.625	Langmuir/PFO	93.943	This work

4.10 Photocatalytic degradation of amoxicillin (AMX)

4.10.1 Influence of pH on photodegradation of AMX

The pH of the solution has a tangible impact on the efficiency of photocatalytic degradation because it modifies the interactions between the pollutants and the photocatalyst as well as the chemical processes that take place during the process. The ionization state of AMX and the zero-charge point (PZC) of g-C_3N_4/Fe_3O_4 are directly influenced by pH, which affects their interaction as well as the rate and effectiveness of degradation. The isoelectric point of amoxicillin is between 2.4 and 7.4. This chemical is either a neutral molecule or exhibits zwitter ionic activity at its isoelectric pH. When pH is less than 2.4, it is positively charged; when pH is greater than 7.4, it is negatively charged (Wahyuni et al., 2024). The best photodegradation of AMX occurs at pH 5, as shown in (figure 4.19a). This state is preferable because the AMX molecules are in the zwitter ionic phase, which also contains both positive and negative functional groups, whereas the g-C_3N_4/Fe_3O_4 photocatalyst has negative charge. After 60 minutes of reaction of 20 mg catalyst dose, 30 mg/L AMX initial concentration, the study suggests that degradation was more effective in an acidic media (53% at pH = 5) than in a basic medium; this could be explained by the acid medium's preference for AMX adsorption on the catalyst's positively charged surface. However, at pH 10, the β-lactam ring is unstable and can break off due to hydrolysis processes, resulting in a small rise in efficiency.

4.10.2 Effect catalyst dosage

The photocatalytic AMX antibiotic degradation at different catalyst dosages were assessed after 40 minutes of exposure to visible light. As the shown in the (figure 4.19b). For the catalyst doses of 25, 50, 75, and 100 mg the corresponding photocatalytic degradation efficiency is 65%, 70%, 65% and 60%. The increasing in photocatalyst dosage, the active sites on the catalyst surface also increased, which in turn increased the amount of ($^{\bullet}OH$) and ($O_2^{\bullet-}$) radicals and degraded drug. The incorporation of a photocatalyst above its optimal concentration can lead to turbidity, resulting in a loss of specific active surface area and lower absorption of light, decreasing degradation capacity due to the overlapping and crowding of catalyst

sample (Zulfiqar et al., 2024). As a result, 0.05 g/L of photocatalyst dose is the optimum amount for this degradation reaction.

4.10.3 Effect of initial concentration

The influence of initial concentration on AMX degradation in aqueous solutions at different concentrations-level was studied in the ensuring research investigation. The catalytic nature and the presence of functional groups are related to the initial concentration parameter. The 2D g-C_3N_4/magnetite nanocomposite, magnetic nanoparticles, and g-C_3N_4 all possess enrich in different functional groups. At low concentrations, degradation of AMX is faster due to more available active sites and radicals. Since the catalyst has a limited number of active sites as AMX concentrations rise those sites get fully occupied, and excess AMX molecules cannot be degraded efficiently due to absorbance of more light themselves, which reduces the amount of light reaching the photocatalyst surface.

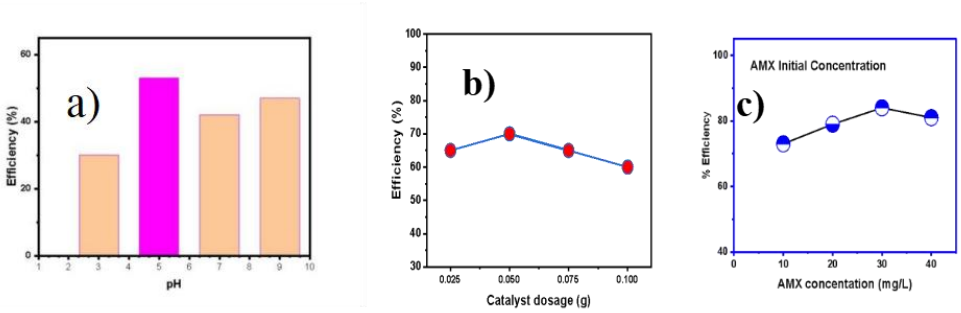

Figure 4.17 Effect of a) pH b) catalyst dose c) initial concentration on photocatalysis

4.10.4 Effect of contact time and catalyst comparison

As shown in (Figure 4.20d) the photodegradation efficiency increases as the light illumination time increases until it gets closer the optimum time. Both the improved interaction between the amoxicillin antibiotic and the OH radicals and the improved contact between the photocatalyst (Fe_3O_4, C_3N_4 and C_3N_4/Fe_3O_4) and the light are responsible for this improvement. The generation of e^-/h^+ pairings are also generated more when reaction times are higher. However, the photocatalyst may approach saturation and achieve comparatively constant efficiency if the irradiation duration is continued. Additionally, the production of degradation products in solution at a

prolonged time in the photodegradation process prevents OH radicals and amoxicillin from interacting.

In the presence of catalysts, exposing AMX solution with visible light indicating in lowering the absorbance with illumination time, indicating photodegradation of the AMX. As shown in (Figure 4.20 c and e), the g-C_3N_4/Fe_3O_4 MNSs suggested enhanced photocatalytic performance in comparison to the pristine 2D CN NPs, with an efficiency of 85.7% for 2D g-C_3N_4/Fe_3O_4 NCs , 76.5% for g-C_3N_4 and 70.8% Fe_3O_4. The result indicated that at optimum reaction condition (pH 5, 0.050 mg/L dose, 30 mg/L initial AMX concentration, in 100 min light illumination time) the heteojunction CN/Fe_3O_4 exihibit better performance for light based degradation of AMX in aquous media.

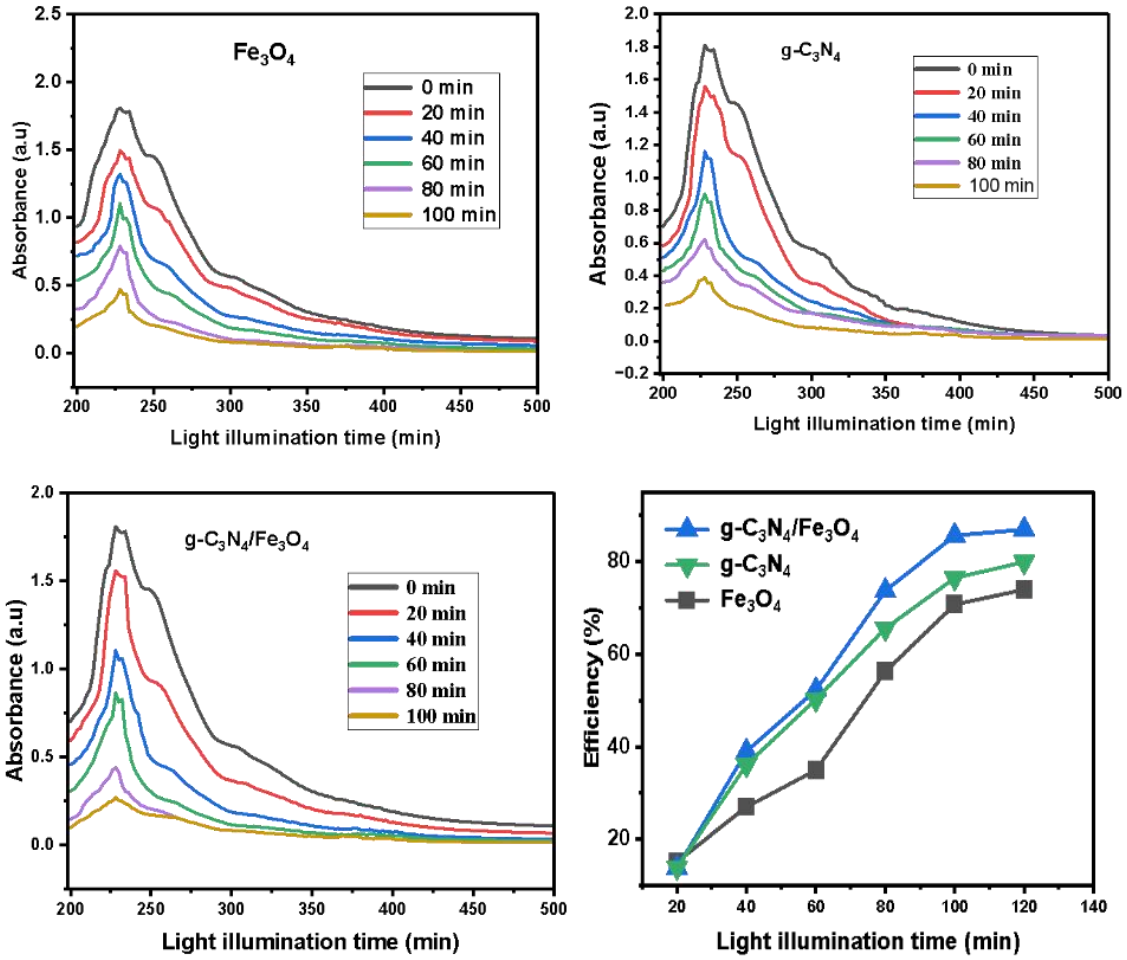

Figure 4.18 Effect of contact time and catalyst comparison based on efficiency at optimum condition

4.10.5 Effect of magnetic field on AMX photodegradation

The AMX removal efficiency of CN/Fe_3O_4 is raised from 85.7 to 94.7 when 0.5T external magnetic fields were exerted during the reaction at optimum condition as seen in figure 4.21. This enhancements may due to the applied external magnetic force on electron spin configuration of a catalyst influences its electronic stability and configuration, which has significant effects on the amount of photogenerated charges,which increasing the photocatalytic efficiency. The Lorentz force produced by the magnetic force also enhanced charge transfer and reducing electron and hole pair recombination.

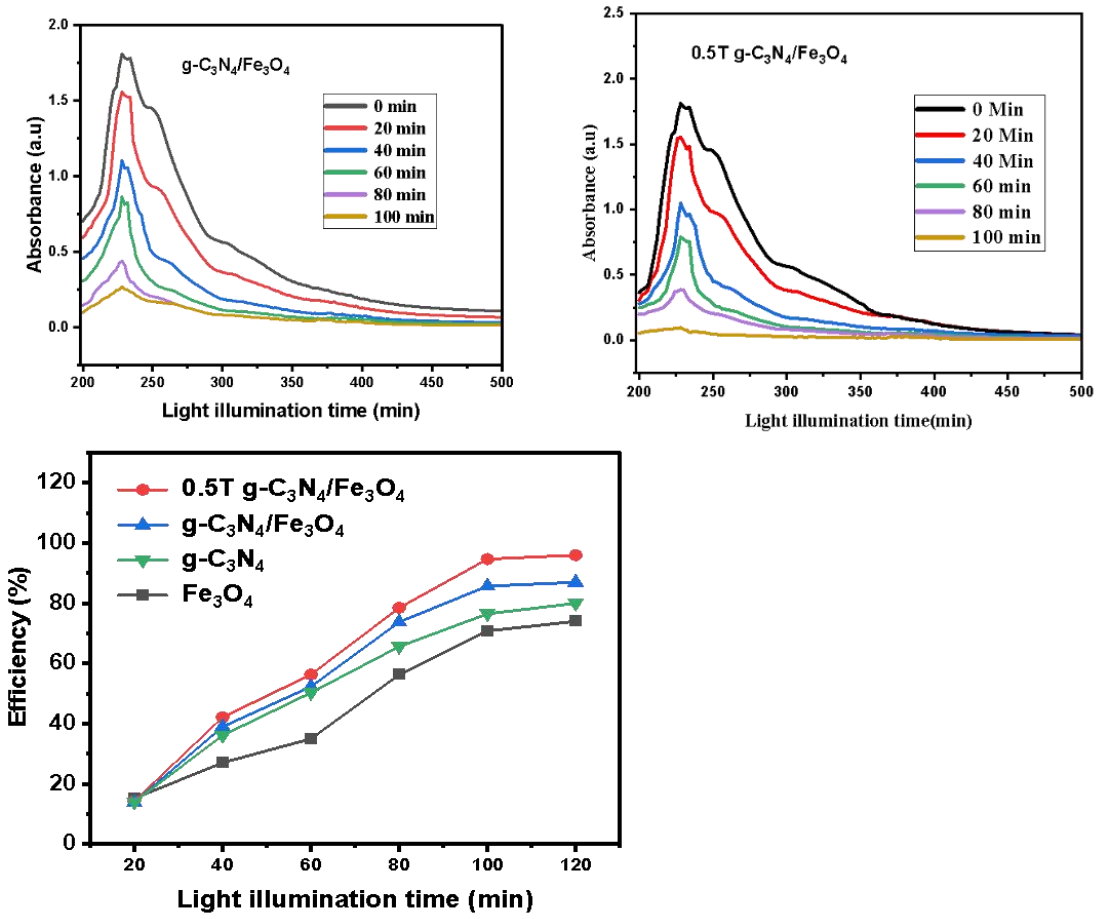

Figure 4. 19 Influence of 0.5T magnetic field on AMX photodegradation

4.10.6 Kinetic study of photodegradation of Amoxicillin

It was concluded that the photocatalytic removal of the AMX antibiotic with 2D CN/Fe_3O_4 MNSs follows pseudo firstorder(PFO) kinetics, and the equation(eqn. 4.6) can be used to calculate the rate constants (Feyie et al., 2024).

$$\ln\frac{C}{Ct} = kt \qquad 4.6$$

The $\ln(C_t/C_0)$ graphs were plotted against time in order to determine the order of the photodegradation reaction. The pseudo first order model was utilized to evaluate the rate of AMX degradationon, with correlation R^2 values of 0.977, 0.972, 0.982, and 0.925 for 0.5T g-C_3N_4/Fe_3O_4 magnetic enhance nanocomposites, g-C_3N_4/Fe_3O_4 NCs, 2D g-C_3N_4 nanosheet and Fe_3O_4 MNPs, respectively. The results show how well the experimental result and the PFO kinetics match, highlighting how reliable this model is at analyzing the degradation process. The PFO rate constant PS degradation using CN/Fe_3O_4 MNSs is get raised in presence of 0.5T applied MF. Which may indicate that the MF enhance rate of MPs photodegradation in addition to increasing its efficiency.

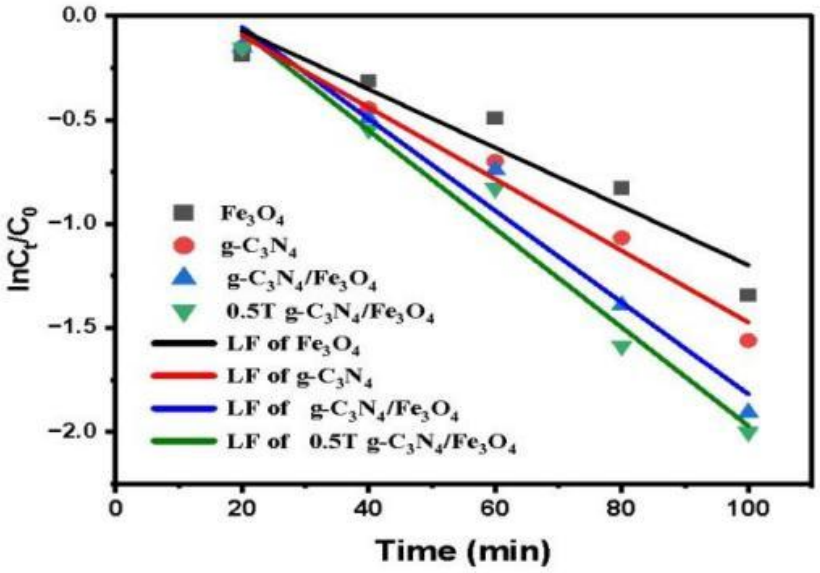

Figure 4.20 Kinetics of photodegradation

Table 4.6 Parameters of PFO kinetics

Catalyst	**K (min^{-1})**	**R^2**	**degradation (%) after 100 min of irradiation**
Fe_3O_4	0.014	0.925	70.8
g-C_3N_4	0.0172	0.982	76.5
g-C_3N_4/Fe_3O_4	0.022	0.972	85.4
0.5T g-C_3N_4/Fe_3O_4	0.02368	0.977	94.7

4.10.6 Reusability tests and comparision of catalyst with other findings

A catalyst's durability and reusability are important considerations when assessing its suitability for industrial use. As a result, we carefully evaluated the nanophotocatalyst's long-term performance and recyclability. By degrading AMX for up to four cycles in visible light under the same scenarios, this tested for the 1:1 g-C_3N_4 /Fe_3O_4 magnetic catalyst. After magnetically separating it from the solution, the catalyst was then rinsed with a 2:1 ethanol and distilled water mixture, dried at 70 °C, and then dispersed in a fresh antibiotic solution for another cycle. As a result, the photocatalytic efficiency of g-C_3N_4/Fe_3O_4 nanostructure in acidic medium (pH = 5) decreased from 85.5%, 80.6%, 74.2%, and 70% at first, second, third and fourth cycles respectively. For 0.5T Magnetic force g-C_3N_4/Fe_3O_4 magnetic enhanced nanostructures, the photocatalytic performance at similar condition with composite, and decrease from 94.7, 87, 80, and 70 at four cycle.

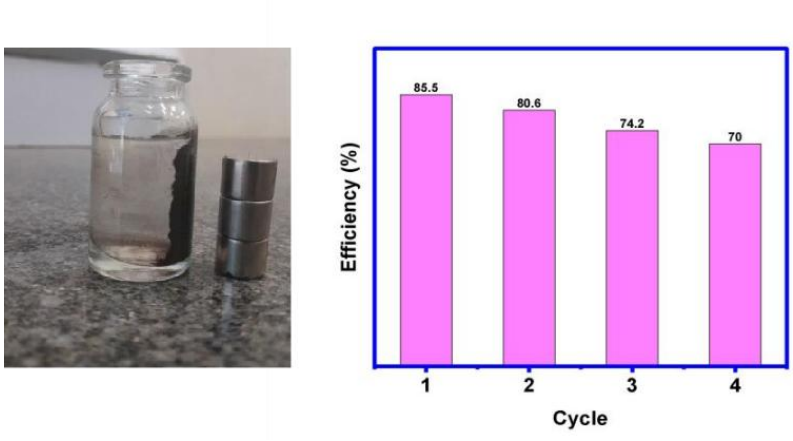

Figure 4. 21 a) Magnetic separation for reusability b) reusability test

Table 4.7 shows a comparison of the synthesized C_3N_4/Fe_3O_4 photocatalysts' achieved degradation efficiency with findings that have already been studied. This studies revealed that the C_3N_4/Fe_3O_4 nanostructure prepared using an easy and cost effective coprecipitation method, has one of the greatest photodegradation capacity for AMX antibiotic removal.

The magnetic CN/Fe_3O_4 produced exhibit comparable or even better photocatalytic performance than the previously published literature values based on their rate constants and efficiency. The illumination time taken (100 min) to degrade 85% even faster than reported literature as summarized (Table 4.7). The AMX degradation rate constant of 0.022 min^{-1} with efficiency 85% in absence of MF and 0.2368 min^{-1} with 94% in RMF suggesting the synthesized catalyst is significant in removal of antibiotics from water environment.

Table 4.7 comparison of synthesized catalyst with previous reported literature.

Catalyst	**dose (mg)**	**AMX mg/L**	**Time min**	**Rate constant**	**Efficency (%)**	**Ref.**
$FeMoO_4/CS/CdO$	40	10	60	0.0222	90.8	(Arul et al., 2025)
$Biochar/Fe_3O_4$	120	100	240	0.0004	74.4	(Zulfiqar et al., 2024)
$ZnO\text{-}TiO_2$	100,	40	210	0.0253	94	(Charafi et al., 2025)
C_3N_4/Fe_3O_4	50	30	100	0.022	85.4	This work
0.5T C_3N_4/Fe_3O_4	50	30	100	0.02368	94.7	This work

4.11 Photocatalytic and external magnetic field enhanced catalytic mechanism

Figure 4.24 illustrates the processes of electron transfer and the generationof the fast degrading molecule or redox process under photocatalytic operation and Equations xx can be used to determine g-C_3N_4 and Fe_3O_4's band point position values.

$$EVB = X - Ee + 0.5Eg \qquad 4.6$$

$$ECB = EVB - Eg \qquad 4.7$$

Where, EVB is valance band potentials, ECB is conduction band potential location, Eg is band gap, and X is an electronegativity on the NHE scale.

Electron–hole pairs are generated on the surface of the 2D C_3N_4/Fe_3O_4 nanostructures, when visible light is penetrated by a 150W hollow cathode lamp. In photocatalysis mechanisms, the holes migrate from a higher to a lower band edge potential while the electrons can move from a lower to a higher band edge potential. As a result, when electrons are produced and excited by the Fe_3O_4 conduction band in this composite, the holes created in its valence band migrate to the g-C_3N_4 valence band, while the electrons released in the g-C_3N_4 conduction band move to the Fe_3O_4 conduction band. The holes in the valance band of g-C_3N_4 produce radicals through an oxidation reaction with water (H_2O), whereas the photogenerated electrons in the conduction band of Fe_3O_4 form peroxide radicals through a reduction reaction with oxygen molecules (O_2) from the air. As soon as AMX antibiotic reacts with these highly powerful radicals, it breaks down the AMX pollutant into CO_2 and water as depicted in figure 4.24

The redox reaction or reactive oxygen species generation and electron-hole and charge progagation processes during photocatalytic activities are as follows:

$$Fe_3O_4 + g{-}C_3N_4 + hv \rightarrow g{-}C_3N_4/Fe_3O_4\,(e^-/h^+) \qquad 4.8$$

$$g{-}C_3N_4\,(e^-) \rightarrow Fe_3O_4\,(c_B) \qquad 4.9$$

$$Fe_3O_4\,(h^+) \rightarrow g\text{-}C_3N_4\,(V_B) \qquad 4.10$$

$$Fe_3O_4\,(e^-) + O_2 \rightarrow O_2^{*-} \qquad 4.11$$

$$g - C_3N_4\,(h^+) + H_2O \rightarrow OH^* + H^{+*} \qquad 4.12$$

$$OH^{*} + O_2^{*-} \text{ AMX antibiotic} \rightarrow \text{INT.} + H_2O + CO_2 \qquad 4.13$$

The photogenerated holes in the VB of g-C_3N_4 react with atmospheric moisture to produce H^+ and OH*, while O_2 molecules from the air/water combine with the freely moving light-generated electrons in Fe_3O_4 CB to form peroxide radicals O_2^{*-} during the photocatalytic reaction, as shown by (Figure 4.22 and eqn, 4.8-4.12). TheOH*, O_2^{*-} free-radicals are a stronger to degrade amoxicillin antibiotic.

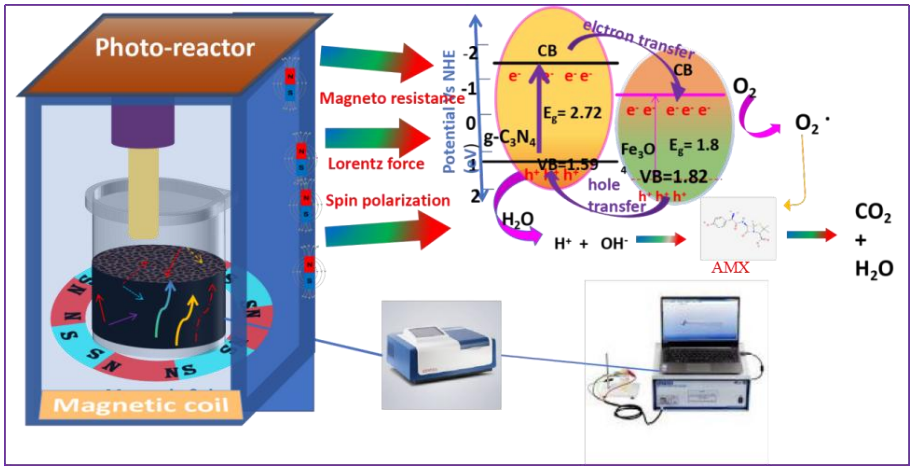

Figure 4. 22 Photocatalysis and electron transfer mechanisms

As shown in the figure 4.24 The applied external magnetic force on electron spin configuration of a catalyst influences its electronic stability and configuration, which has significant effects on the amount of photogenerated charges,which increasing the photocatalytic efficiency. The Lorentz force produced by the magnetic force also enhanced charge transfer and reducing electron and hole pair recombination. The main reason for enhancements of photodegradation reaction is due to transformation, migration and extended life time of free radical oxygen based reactive species's. Such free radicals might include light-induced electrons(Lo et al.) in Fe_3O_4 conduction band, hole (h^+) travel from Fe_3O_4 valance band to g-C_3N_4 valance band, hydroxyl radicals ($OH^·$), superoxide radicals ($O_2^·$), and other free radical component.

5 Conclusion and Recommendation

5.1 Conclusion

In this study, Fe_3O_4, 2D C_3N_4 and 2D C_3N_4/Fe_3O_4 MNSs were prepared by cost effective, easy and efficient thermal polymerization followed co-precipitation methods. XRD characterization clearly shows that the distribution of Fe_3O_4 MNPs was successfully loaded on the surface of 2D C_3N_4 nanostructures, with better crystall structure, which is further confirmed by by the FTIR , FESEM and SEM-EDX analysis. The distribution of Fe_3O_4 to C_3N_4 exhibited in formation of n-n heterojunction, which boosted the degradation of amoxicillin 85.4% after 100 min uv-light treatment, and due to higher of surface area and porosity, the C_3N_4/Fe_3O_4 magnetic nanocomposite show highest adsorption capacity 433.05 mg/g than pristine C_3N_4 (327.16mg/g) and Fe_3O_4 (216.2 mg/g) against polystyrene microplastic removal from water environment.

In this study the enhancement of photocatalysis and adsorption with external magnetic field were also carefully investigated. Interestingly the synergistic effect of 0.5T MF with n-n g-C_3N_4/Fe_3O_4 displayed the highest catalytic activity, with a notable 94.7% degradation of AMX achieved. In addition presence of these non-contact external magnetic force also boost adsorption capacity of C_3N_4/Fe_3O_4 to 464.6 mg/g at optimum conditions.This enhancements mainly described by improving charge separation and reducing recombination of photogenerated electrons and holes. This enhancement occurs through several mechanisms: increasing electron spin polarization, promoting the Lorentz force on charged carriers, and inducing magnetohydrodynamic (MHD) effects for better mass transfer. The successful reuse of the catalyst, retaining over 70% efficiency even after four consecutive cycles for both photocatalysis and adsorption, demonstrates its stability and reusability, supporting its practical and large-scale application. Therefore, these findings suggest the potential of Fe_3O_4/C_3N_4 nanostructures as multifunctional catalysts for the effective removal of antibiotic and microplastic pollutants from water systems.

5.2 Recommendations

For the future study there are few recommendation related large-scale device fabrication of synthesized catalyst to support industrial-level deployment and and application in real water analysis. Research should also focus on optimizing magnetic field intensity to maximize photocatalytic and adsorptive efficiency, especially under dynamic or continuous-flow conditions. Furthermore, other non-contact external forces such as electric fields, ultrasound,Microwave radiation or light modulation should be investigated to compare their enhancement effects with magnetic fields, allowing for a more comprehensive understanding of controllable external forces in advanced water treatment technologies.

Reference

AbuMousa, R. A., Khezami, L., Ismail, M., Ben Aissa, M. A., Modwi, A., & Bououdina, M. (2022). Efficient mesoporous MgO/g-C_3N_4 for heavy metal uptake: modeling process and adsorption mechanism. *Nanomaterials*, *12*(22), 3945.

Ai, Q., Yuan, Z., Huang, R., Yang, C., Jiang, G., Xiong, J., Huang, Z., & Yuan, S. (2019). One-pot co-precipitation synthesis of Fe_3O_4 nanoparticles embedded in 3D carbonaceous matrix as anode for lithium ion batteries. *Journal of Materials Science*, *54*(5), 4212-4224.

Alahmadi, N. (2022). Recent progress in photocatalytic removal of environmental pollution hazards in water using nanostructured materials. *Separations*, *9*(10), 264.

Ali, M. A., & Maafa, I. M. (2024). Photodegradation of amoxicillin in aqueous systems: A review. *International journal of molecular sciences*, *25*(17), 9575.

Arul, V., Radhakrishnan, K., Kasthuri, N., Vadivu, D. S., Kumar, J. V., Nivetha, M. S., Mythili, R., & Devanesan, S. (2025). Visible-Light-Driven Photocatalytic Degradation of Amoxicillin Using $FeMoO_2$/Chitosan/CdO Nanocomposite for Sustainable Water Treatment. *Polymers for Advanced Technologies*, *36*(2), e70097.

Bai, G., Wang, C., Wang, B., Promcharoen, P., Chumkaeo, P., & Somsook, E. (2025). Sustainable Adsorption of Polystyrene Microplastics in Aqueous Media Using PET-C Synthesized from Plastic Waste: DFT and Experimental Studies. *ACS Sustainable Chemistry & Engineering*.

Bai, X., Chen, W., Wang, B., Sun, T., Wu, B., & Wang, Y. (2022). Photocatalytic degradation of some typical antibiotics: Recent advances and future outlooks. *International journal of molecular sciences*, *23*(15), 8130.

Bian, Y., Zheng, G., Ding, W., Hu, L., & Sheng, Z. Magnetic field effect on the photocatalytic degradation of methyl orange by commercial TiO_2 powder, RSC Adv. 11 (2021) 6284–6291. In.

Bian, Y., Zheng, G., Ding, W., Hu, L., & Sheng, Z. (2021). Magnetic field effect on the photocatalytic degradation of methyl orange by commercial TiO_2 powder. *RSC advances*, *11*(11), 6284-6291.

Capodaglio, A. G. (2025). Micro-and Nano-Plastics in Drinking Water: Threat or Hype? Critical State-of-the-Art Analysis of Risks and Approaches. *Journal of Xenobiotics*, *15*(3), 85.

Charafi, S., Janani, F. Z., Elhalil, A., Abdennouri, M., Sadiq, M., & Barka, N. (2025). Optimization of photocatalytic degradation of amoxicillin by ZnO-TiO_2 heterojunction under UV-Visible irradiation. *Cleaner Chemical Engineering*, 100183.

Cojocaru, V. C., Cristea, I. N., Paris, I. A., Ionescu, I. A., & Chiriac, F. L. (2024). Exploring sustainable solutions: Dynamic adsorption, isotherm models, and kinetics of organic contaminants on polystyrene microplastics. *Sustainability*, *16*(17), 7743.

Dan, H., Kong, Y., Yue, Q., Liu, J., Xu, X., Kong, W., Gao, Y., & Gao, B. (2021). Magnetic field-enhanced radical intensity for accelerating norfloxacin degradation under FeCu/rGO photo-Fenton catalysis. *Chemical Engineering Journal*, *420*, 127634.

Dhanalakshmi, R., Denardin, J. C., Sreekanth, T., Reddeppa, M., Rosaiah, P., Yoo, K., & Kim, J. (2023). Synergistic magnetic field-photocatalysis for the concurrent removal of inorganic and organic contaminants over $PrFeO_3$/ZnO heterostructures. *Inorganic Chemistry Communications*, *156*, 111189.

Ding, N., Wang, Y., Shen, Z., Liu, H., Li, Y., & Sun, Y. (2025). Mechanisms and application of magnetic field enhancing pollutant adsorption in water: A review. *Separation and Purification Technology*, *356*, 129938.

Duan, J., Zhao, L., Lv, W., Li, Y., Zhang, Y., Ai, S., & Zhu, L. (2019). Facile synthesis of g-C_3N_4/Fe_3O_4 nanocomposites for fluorescent detection and removal of Cr (VI). *Microchemical Journal*, *150*, 104105.

Fang, Y., Zheng, Y., Fang, T., Chen, Y., Zhu, Y., Liang, Q., Sheng, H., Li, Z., Chen, C., & Wang, X. (2020). Photocatalysis: an overview of recent developments and technological advancements. *Science China Chemistry*, *63*(2), 149-181.

Feyie, E. K., Zereffa, E. A., Tadesse, A., Goddati, M., Noh, D., Oh, E., Tufa, L. T., & Lee, J. (2024). An Efficient p–n Heterojunction Copper Tin Sulfide/g-C3N4 Nanocomposite for Methyl Orange Photodegradation. *ACS omega*, *9*(26), 28463-28475.

Gao, W., Lu, J., Zhang, S., Zhang, X., Wang, Z., Qin, W., Wang, J., Zhou, W., Liu, H., & Sang, Y. (2019). Suppressing photoinduced charge recombination via the Lorentz force in a photocatalytic system. *Advanced Science*, *6*(18), 1901244.

García-Rollán, M., Sanz-Santos, E., Belver, C., & Bedia, J. (2025). Key adsorbents and influencing factors in the adsorption of micro-and nanoplastics: A review. *Journal of Environmental Management*, *383*, 125394.

Giri, S., Lamichhane, G., Khadka, D., & Devkota, H. P. (2024). Microplastics contamination in food products: Occurrence, analytical techniques and potential impacts on human health. *Current Research in Biotechnology*, *7*, 100190.

González Vázquez, O. F., Moreno Virgen, M., Esparza González, M., Hernández Montoya, V., Tovar-Gómez, R., & Durán Valle, C. J. (2020). Analysis of the effect of a magnetic field applied to a process of adsorption of water contaminants using adsorbents of different magnetic orderings. *Industrial & Engineering Chemistry Research*, *59*(30), 13820-13830.

Grafton, R. Q., Fanaian, S., Horne, J., Katic, P., Nguyen, N.-M., Ringler, C., Robin, L., Talbot-Jones, J., Wheeler, S. A., & Wyrwoll, P. R. (2025). Rethinking responses to the world's water crises. *Nature Sustainability*, *8*(1), 11-21.

Grbic, J., Nguyen, B., Guo, E., You, J. B., Sinton, D., & Rochman, C. M. (2019). Magnetic extraction of microplastics from environmental samples. *Environmental Science & Technology Letters*, *6*(2), 68-72.

Heo, Y., Lee, E.-H., & Lee, S.-W. (2022). Adsorptive removal of micron-sized polystyrene particles using magnetic iron oxide nanoparticles. *Chemosphere*, *307*, 135672.

Indhur, R., Kumar, A., Bux, F., & Kumari, S. (2025). Efficient Microplastic Removal from Wastewater using Fe_3O_4 Functionalized g-C_3N_4 and BNNS: A Comprehensive Study. *Journal of Environmental Chemical Engineering*, 117145.

Karunattu Sajan, M., Kirubalan, M. R., Rajendran, A. S., & Natesan, A. L. F. (2024). Exploring the effective adsorption of polystyrene microplastics from aqueous solution with magnetically separable nickel/reduced graphene oxide (Ni/rGO)

nanocomposite. *Environmental Science and Pollution Research*, *31*(26), 38099-38116.

Li, J., Pei, Q., Wang, R., Zhou, Y., Zhang, Z., Cao, Q., Wang, D., Mi, W., & Du, Y. (2018). Enhanced photocatalytic performance through magnetic field boosting carrier transport. *ACS nano*, *12*(4), 3351-3359.

Li, K., Chen, M., Chen, L., Zhao, S., Xue, W., & Han, Y. (2023). Synthesis and application of a $Fe_3O_4/Ag_3PO_4/g\text{-}C_3N_4$ magnetic composite photocatalyst for sulfonamide antibiotics degradation. *Sustainability*, *15*(17), 13279.

Liang, F.-Y., Huang, H.-W., Chen, Y.-C., & Huang, P.-J. (2025). Enhanced Solar-Driven Photocatalysis with CuTCPP/g-C_3N_4 for Hydrogen Production and Environmental Remediation. *Energy & Fuels*, *39*(13), 6533-6548.

Liu, P., & Mao, X. (2025). Photocatalytic Performance Enhancement Using External Magnetic Fields-A Review. *Advanced Materials Interfaces*, *12*(17), e00493.

Lo, F. F., Kow, K.-W., Kung, F., Ahamed, F., Kiew, P.-L., Yeap, S.-P., Chua, H.-S., Chan, C.-H., Yusoff, R., & Ho, Y. K. (2021). Effect of magnetic field on nano-magnetite composite exhibits in ion-adsorption. *Science of the Total Environment*, *780*, 146337.

Lu, H.-C., Ziajahromi, S., Neale, P. A., & Leusch, F. D. (2021). A systematic review of freshwater microplastics in water and sediments: recommendations for harmonisation to enhance future study comparisons. *Science of the Total Environment*, *781*, 146693.

Ma, J., Chen, Y., Zhou, G., Ge, H., & Liu, H. (2024). Recent advances in photocatalytic degradation of tetracycline antibiotics. *Catalysts*, *14*(11), 762.

Ma, J., Ding, N., & Liu, H. (2023). Research progress in photocatalytic activated persulfate degradation of antibiotics by bismuth-based photocatalysts. *Separation and Purification Technology*, *324*, 124628.

Ma, L. (2025). Understanding the Distribution, Sources and Risks of Antibiotic Resistance Contamination in Drinking Water Systems: Research Needs to Reduce Emerging Pollutants and Mitigate Public Health Risks. *Environmental Science & Technology Letters*, *12*(3), 248-250.

Matar, G. H., Dikbas, C., & Andac, M. (2024). Efficient magnetic adsorption of polystyrene nanoplastic from aqueous solutions by eco-friendly Fe_3O_4

nanoparticles: Removal, kinetic and isotherm modeling studies. *Journal of Environmental Health Science and Engineering*, *23*(1), 4.

Meng, S., Li, Y., Liu, Y., Zhan, S., Ma, Q., & Li, Y. (2023). Recent advances and mechanisms in magnetic field enhanced photocatalysis: A review. *Environmental Surfaces and Interfaces*, *1*, 10-23.

Nejat, R. (2024). Enhancing the photocatalytic efficiency of g-C_3N_4 for ciprofloxacin degradation using Tetrakis (acetonitrile) copper (I) hexafluorophosphate as a highly effective cocatalyst. *Heliyon*, *10*(16).

Nugroho, D., Joo, Y. J., Cho, K. Y., Benchawattananon, R., Chanthai, S., & Oh, W.-C. (2025). Synergistic magnetic field effect to enhance photocatalytic effect for pharmaceutics degradation by Ti_3C_2 MXene/GQDs@ ZnO. *Journal of Photochemistry and Photobiology A: Chemistry*, *462*, 116224.

Pei, M., Fan, J., Zhang, C., Xu, J., Yang, Y., Wei, H., Zhang, C., Zhu, L., & Gao, P. (2025). Antibiotic and microplastic co-exposure: Effects on Daphnia magna and implications for ecological risk assessment. *Critical Reviews in Environmental Science and Technology*, *55*(5), 287-309.

Ren, J., Zhu, Z., Qiu, Y., Yu, F., Zhou, T., Ma, J., & Zhao, J. (2021). Enhanced adsorption performance of alginate/MXene/CoFe2O4 for antibiotic and heavy metal under rotating magnetic field. *Chemosphere*, *284*, 131284.

Sanz-Santos, E., Alvarez-Montero, A., Gomez-Aviles, A., Belver, C., & Bedia, J. (2025). Adsorption of polystyrene nanoplastics on sawdust-based activated carbons. *Journal of Water Process Engineering*, *69*, 106891.

Sarp, G., & Yilmaz, E. (2022). g-C_3N_4@ TiO_2@ Fe_3O_4 multifunctional nanomaterial for magnetic solid-phase extraction and photocatalytic degradation-based removal of trimethoprim and isoniazid. *ACS omega*, *7*(27), 23223-23233.

Selen, V., Guler, O., Nodehi, M., Sarı, A., Yaras, A., Gencel, O., Gholampour, A., & Ozbakkaloglu, T. (2023). Physical-Mechanical and Electrical Resistivity Properties of Cementitious Mortars Containing Fe_3O_4-MWCNTs Nanocomposite. *Sustainability*, *15*(14), 11045.

Shi, X., Zhang, X., Gao, W., Zhang, Y., & He, D. (2022). Removal of microplastics from water by magnetic nano-Fe_3O_4. *Science of the Total Environment*, *802*, 149838.

Sousa, M. A., Gonçalves, M. A., Sales, T. A., Lino, J. B. d. R., de Moura, S. G., da Silva, J. P., & Ramalho, T. C. (2025). Influence of Magnetic Field on Atrazine Adsorption and Degradation by Ferroxite and Hematite. *Magnetism*, *5*(2), 11.

Sun, N., Si, X., He, L., Zhang, J., & Sun, Y. (2024). Strategies for enhancing the photocatalytic activity of semiconductors. *International Journal of Hydrogen Energy*, *58*, 1249-1265.

Wahyuni, E. T., Cahyono, R. N., Nora, M., Alharissa, E. Z., & Kunarti, E. S. (2024). Degradation of amoxicillin residue under visible light over TiO_2 doped with Cr prepared from tannery wastewater. *Results in Chemistry*, *7*, 101302.

Wang, C., Zhao, J., & Xing, B. (2021). Environmental source, fate, and toxicity of microplastics. *Journal of hazardous materials*, *407*, 124357.

Wang, Y., Yang, Y., Liu, X., Zhao, J., Liu, R., & Xing, B. (2021). Interaction of microplastics with antibiotics in aquatic environment: distribution, adsorption, and toxicity. *Environmental Science & Technology*, *55*(23), 15579-15595.

Wang, Z., Xu, L., Cai, X., & Yu, T. (2024). Low-energy photoresponsive magnetic-assisted cleaning microrobots for removal of microplastics in water environments. *ACS Applied Materials & Interfaces*, *16*(45), 61899-61909.

Wudil, Y., Ahmad, U., Gondal, M., Al-Osta, M. A., Almohammedi, A., Sa'id, R., Hrahsheh, F., Haruna, K., & Mohamed, M. (2023). Tuning of graphitic carbon nitride (g-C_3N_4) for photocatalysis: a critical review. *Arabian Journal of Chemistry*, *16*(3), 104542.

Yang, J., Chen, H., Gao, J., Yan, T., Zhou, F., Cui, S., & Bi, W. (2016). Synthesis of Fe_3O_4/g-C_3N_4 nanocomposites and their application in the photodegradation of 2, 4, 6-trichlorophenol under visible light. *Materials Letters*, *164*, 183-189.

Yuan, F., Yue, L., Zhao, H., & Wu, H. (2020). Study on the adsorption of polystyrene microplastics by three-dimensional reduced graphene oxide. *Water Science and Technology*, *81*(10), 2163-2175.

Zulfiqar, N., Nadeem, R., & Musaimi, O. A. (2024). Photocatalytic degradation of antibiotics via exploitation of a magnetic nanocomposite: a green nanotechnology approach toward drug-contaminated wastewater reclamation. *ACS omega*, *9*(7), 7986-8004.

Apendix

1. The simulate magnet used through this study and magnetic properties of prepared CN/Fe_3O_4 naostructure

Appendix Figure 1 a) simulated magnet b) CN/Fe_3O_4 after exposed 2 min near magnet

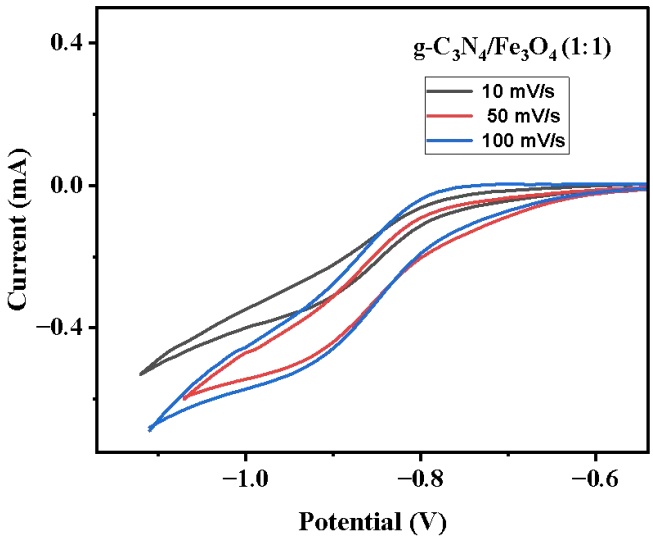

Appendix Figure 2. (a) Cycilic voltammograms of g-C_3N_4/Fe_3O_4 plotted at a different scan rate , in 1 M KOH aqueous solution.